Chemical Science

ROYAL SOCIETY OF CHEMISTRY

REVIEW

View Article Online
View Journal | View Issue

Cite this: *Chem. Sci.*, 2025, **16**, 13594

Bulk and interface engineering of Prussian blue analogue cathodes for high-performance sodium-ion batteries

Boao Zhou,†[a] Yun Gao,†[c] Xihao Lin,[bc] Bin Yang,[bc] Ning Kang,[bc] Yun Qiao,[a] Hang Zhang,*[bc] Li Li*[ac] and Shulei Chou*[bc]

Prussian blue analogues (PBAs) possess a unique three-dimensional crystal structure, which provides ample space for the movement of sodium ions (Na^+), making them an ideal choice for cathode materials in sodium-ion batteries (SIBs). However, the bulk phase of PBAs typically contains some amount of crystal water and vacancies, which compromise the integrity of the lattice and impede the migration of Na^+. Additionally, interface-related issues, such as side reactions and the dissolution of transition metal ions, severely limit the reversible capacity and cycle stability of PBA-based cathode materials. Therefore, addressing these challenges from the bulk and interface of PBAs is critical for the development of high-performance cathode materials for SIBs. This review aims to provide insights into potential strategies for overcoming these limitations and enhancing the electrochemical performance of PBAs. Firstly, the structure, morphology, and reaction mechanisms of PBAs are summarized systematically. The key challenges hindering the commercialization of PBAs are then categorized in this review. Several effective strategies for addressing these challenges are provided, including bulk phase engineering (thermal treatment, element doping, and etching), interface engineering (coating, ion exchange, and electrolyte additives), and the co-regulation of bulk and interface. Finally, the future commercialization prospects of PBAs are discussed, highlighting the necessary steps for transitioning from laboratory-scale research to industrial-scale production.

Received 17th April 2025
Accepted 29th May 2025

DOI: 10.1039/d5sc02819a

rsc.li/chemical-science

1 Introduction

With the increasing emphasis on low-carbon lifestyles and sustainable energy systems, the new energy industry is advancing rapidly.[1,2] Among various energy storage technologies, electrochemical storage, particularly secondary batteries, is preferred for its high efficiency and flexibility.[3,4] While lithium-ion batteries (LIBs) have dominated portable devices and electric vehicles due to their long life-span and high power density, the uneven distribution and scarcity of lithium resources restrict their application in large-scale energy storage systems (ESSs).[5–7] In the process of exploring alternative energy solutions, sodium-ion batteries (SIBs) have been the focus of research due to their abundant resources, low cost, and similar physicochemical properties to LIBs (Fig. 1a).[8–10] Fig. 1b illustrates the rapid increase in research on SIBs, cathode materials, and PBAs over the past decade. With the continuous progress of technology, SIBs are expected to play an important role in ESSs, low-speed electric vehicles, and distributed energy systems, thereby offering innovative solutions to global energy and environmental challenges.[11]

Despite the numerous advantages of SIBs, several challenges remain in their commercialization. One of the main limitations is their relatively low energy density, which is primarily attributed to the slower migration of sodium ions (Na^+) within the sodium storage material. This slow migration is due to the larger molecular weight and ionic radius of Na^+ compared to lithium ions (Li^+). Additionally, the higher redox potential of Na^+/Na (−2.71 V *vs.* standard hydrogen electrode) in comparison to Li^+/Li (−3.04 V *vs.* standard hydrogen electrode) also contributes to the inferior mass/volume energy density of the SIBs. Eqn (1) provides a methodology for calculating the theoretical energy density.[12]

$$E = QV = 26\,800\frac{nV}{M} \quad (1)$$

where E is the theoretical specific energy density, Q is the specific capacity, V is the potential, n is the number of electrons transferred in the reaction, and M is the molecular weight of the

[a]*School of Environment and Chemical Engineering, Shanghai University, Shanghai, 20444, P. R. China. E-mail: LiLi2020@shu.edu.cn*

[b]*Institute for Carbon Neutralization Technology, College of Chemistry and Materials Engineering, Wenzhou University, Wenzhou, Zhejiang, 325035, P. R. China. E-mail: hang@wzu.edu.cn; chou@wzu.edu.cn*

[c]*Wenzhou Key Laboratory of Sodium-Ion Batteries, Wenzhou University Technology Innovation Institute for Carbon Neutralization, Wenzhou, Zhejiang 325035, China*

† B. Z. and Y. G. contributed equally to this work.

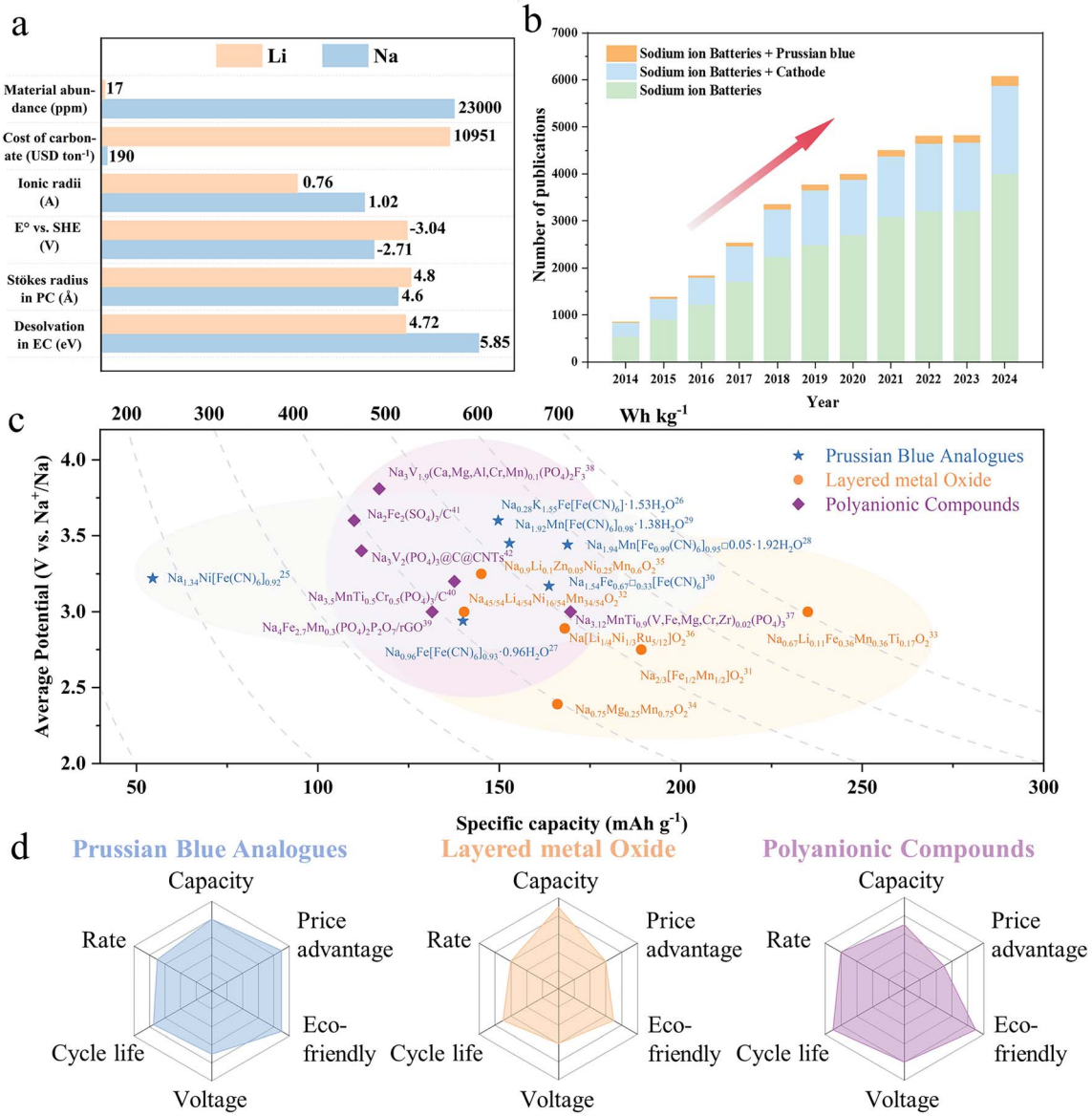

Fig. 1 (a) Comparison between lithium and sodium elements of crustal abundance, raw material costs, ion radius, standard potential, Stökes radius in polypropylene carbonate (PC), and desolvation in ethylene carbonate (EC). (b) The number of publications on SIBs in the past decade (as of December 2024, generated by Web of Science using keywords 'Sodium ion Batteries', 'Sodium ion Batteries and Cathode', 'Sodium ion Batteries and Prussian blue'). (c) The specific capacity and voltage window of SIB cathode materials recently reported. (d) Radar chart of specific capacity, rate performance, cycle life, average voltage, environmental friendliness and price advantage of three cathode materials in SIBs.

material. The output voltage of the battery is due to the potential difference between the anode and cathode. It can be seen that for SIBs, since their molecular weights have been determined, the key to improving energy density is to develop cathode materials with high capacity and high potential. The cathode material is one of the four primary components of a battery, accounting for approximately 30–40% of its total cost. It plays a crucial role in determining both the energy density and cycle life of the battery. Currently, the mainstream cathode materials include layered metal oxides, polyanionic compounds and PBAs. Among them, layered metal oxides have relatively large specific capacity and high operating potential, however, they suffer from a series of fatal problems such as unstable cathode/electrolyte interface, poor air stability, and irreversible phase transition.[13–16] Polyanionic compounds offer excellent safety and long cycle life, but their poor conductivity results in a lower practical specific capacity.[17,18] Compared with these two materials, PBAs show unique advantages, such as high theoretical capacity, low synthesis cost, flexible and adjustable structure. Notably, their oxygen-free structure can circumvent the common risk of thermal runaway of batteries, which makes it one of the highly promising cathode materials in SIBs.[19–21] Fig. 1c, d and Table 1 summarize the performance of three representative cathode materials in terms of specific capacity, rate performance, cycle life, average voltage, price advantage and environmental friendliness. However, in practical

Table 1 Electrochemical performance comparison of three representative cathode materials

Type	Electrodes	Voltage window [V *vs.* Na^+/Na]	Average voltage [V *vs.* Na^+/Na]	Capacity [mA h g^{-1}]/energy density [W h kg^{-1}]	Capacity retention [retention, cycle @ mA g^{-1}]	Ref.
Prussian blue analogues	$Na_{1.34}Ni[Fe(CN)_6]_{0.92}$	2.0–4.3	3.32	54.5/175.49	63.4%, 3000 @ 50	25
	$Na_{0.28}K_{1.55}Fe[Fe(CN)_6]\cdot 1.53H_2O$	2.0–4.2	~3.04	147.9/~450.0	83.5%, 300 @ 150	26
	$Na_{0.96}Fe[Fe(CN)_6]_{0.93}\cdot 0.96H_2O$	2.0–4.0	2.94	140.0/411.6	93.2%, 200 @ 170	27
	$Na_{1.94}Mn[Fe_{0.99}(CN)_6]_{0.95}\square_{0.05}\cdot 1.92H_2O$	2.0–4.2	3.44	168.8/580.7	87.6%, 100 @ 100	28
	$Na_{1.92}Mn[Fe(CN)_6]_{0.98}\cdot 1.38H_2O$	2.0–4.0	3.45	152.8/527.2	82.0%, 500 @ 100	29
	$Na_{1.54}Fe_{0.67}\square_{0.33}[Fe(CN)_6]$	2.0–4.2	~3.10	163.7/~507.5	78.5%, 200 @ 500	30
Layered metal oxides	$Na_{2/3}[Fe_{1/2}Mn_{1/2}]O_2$	1.5–4.2	2.75	189.1/520.0	70.0%, 30 @ 260	31
	$Na_{45/54}Li_{4/54}Ni_{16/54}Mn_{34/54}O_2$	2.0–4.0	3.00	140.3/421.0	75.0%, 500 @ 140	32
	$Na_{0.67}Li_{0.11}Fe_{0.36}Mn_{0.36}Ti_{0.17}O_2$	1.5–4.2	3.00	235.0/705.0	85.4%, 100 @ 200	33
	$Na_{0.75}Mg_{0.25}Mn_{0.75}O_2$	1.5–4.0	2.39	166.0/396.7	83.1%, 500 @ 700	34
	$Na_{0.9}Li_{0.1}Zn_{0.05}Ni_{0.25}Mn_{0.6}O_2$	2.0–4.3	3.25	145.0/471.3	87.0%, 100 @ 20	35
	$Na[Li_{1/4}Ni_{1/3}Ru_{5/12}]O_2$	2.0–4.1	2.89	168.0/485.5	87.0%, 100 @ 260	36
Polyanionic compounds	$Na_{3.12}MnTi_{0.9}(V,Fe,Mg,Cr,Zr)_{0.02}(PO_4)_3$	1.5–4.3	3.00	169.6/508.8	85.6%, 500 @ 176	37
	$Na_3V_{1.9}(Ca,Mg,Al,Cr,Mn)_{0.1}(PO_4)_2F_3$	2.0–4.3	3.81	116.9/445.4	90.2%, 400 @ 0.1C	38
	$Na_4Fe_{2.7}Mn_{0.3}(PO_4)_2P_2O_7$/rGO	1.7–4.3	~3.00	131.5/~394.5	91.6%, 200 @ 258	39
	$Na_{3.5}MnTi_{0.5}Cr_{0.5}(PO_4)_3$/C	1.5–4.3	~3.20	137.6/~440.3	91.2%, 300 @ 100	40
	$Na_2Fe_2(SO_4)_3$/C	2.0–4.3	3.60	110/396.0	N/A	41
	$Na_3V_2(PO_4)_3$@C@CNTs	2.5–4.3	~3.40	112/~380.8	99.9%, 20 000 @ 20 000	42

applications, to achieve high-performance SIBs, further solutions are needed to address some key issues with PBAs, such as low initial coulombic efficiency, poor cycling stability and low charge/discharge specific capacity. Based on the previous research, it has been found that the key problems lie in the following. (1) The presence in the bulk phase of $Fe(CN)_6$ vacancies and lattice water molecules. These vacancies and water molecules were mainly originated from the co-precipitation reaction process as well as the inhomogeneous nucleation rate. Their presence occupies sodium storage sites on the one hand, and alters the local electric field distribution and ionic diffusion paths within the material on the other hand. (2) Irreversible phase transitions and lattice distortions. In particular, in manganese-based PBA systems, the special electronic configuration of manganese ions triggers lattice distortion due to the Jahn–Teller effect.[22] During the charge/discharge process, this distortion leads to an unstable structure. The frequent irreversible phase transition destroys the crystal structure of the material, which seriously weakens its cycling stability and charge/discharge specific capacity. (3) Side reactions present at the interface. At the contact interface between PBAs and other components such as the electrolyte, all kinds of side reactions are likely to occur.[23,24] These side reactions not only consume active substances, but also damage the stability and integrity of the interface, hindering the smooth transmission of ions and electrons at the interface, which ultimately leads to a significant reduction in the actual capacity and cycling performance of PBAs.

To address these challenges faced by PBAs in current applications, researchers have actively explored and implemented a range of effective regulation strategies; these strategies include structural, morphological, and surface modifications, which can alter the chemical composition and skeletal structure of PBAs, and then optimizing their intrinsic properties. Alternatively, other materials can be used to coat PBAs to enhance the stability of the interface. The review firstly thoroughly introduces the crystal structure and electrochemical reaction mechanisms of PBAs, followed by a discussion on the current commercialization process and the challenges facing future development. Key factors affecting the practical applications of PBAs are highlighted, including crystal water, crystal defects, side reactions, transition metal dissolution, low conductivity, and structural collapse during cycling. This review addresses the challenges hindering the commercialization of PBAs by categorizing their regulation strategies into two main areas: bulk phase regulation and interface regulation. Bulk phase regulation focuses on the material itself and aims to improve the intrinsic properties of PBAs, including the control of crystal water content and vacancies. Interface regulation examines the interactions between the PBAs and their external environment, with particular emphasis on the interfacial properties between the material and the surrounding medium, such as the electrolyte and collector. The complementary approach of bulk phase and interface regulation provides a comprehensive and effective solution to the obstacles currently limiting the commercialization of PBAs. Several low-cost, scalable structural regulation methods that can be applied in practical production are introduced, such as bulk doping, defect control, etching, coating, surface ion exchange, and the use of additives. Finally, the future development of PBAs is explored, with the aim of providing valuable insights to promote their commercialization.

2 The fundamentals of PBAs in SIBs

2.1 Crystal and phase structures

Prussian blue (PB), the first synthetic coordination compound in history, has been extensively studied for its unique

physicochemical properties since its discovery in 1704.[43] The chemical formula of an ideal PBA can be expressed as $A_xM_A[M_B(CN)_6]_y\cdot\square_{1-y}\cdot nH_2O$. In this formula, 'A' represents alkali metal ions (*e.g.*, Li, Na, K), 'M_A' and 'M_B' are transition metal ions (*e.g.*, Fe, Mn, Co, Ni, Cu), '□' indicates $Fe(CN)_6$ vacancies, and 'H_2O' denotes crystal water, including adsorbed water, interstitial water, and coordination water (Fig. 2a).[44] Fig. 2b and c show the perfect crystal structure of PBAs and a defective crystal structure containing crystal water and defects. Overall, the values of 'x', '$1-y$' and 'n' depend on the synthesis conditions, including the liquid phase environment and the presence of chelating agents. In different liquid phase systems, such as acidic, alkaline or neutral solution environments, the ions can exist in very different forms, reactivity and mode of interaction. For example, chelating agents can form stable complexes with metal ions, changing the effective concentration and reactivity of the metal ions. As a result, the rate and mode of their participation in PBA synthesis reactions are altered. These changes ultimately affect three aspects of the final product: the alkali metal content, the number of vacancies, and the amount of crystal water.[45] It is worth noting that a high proportion of crystal water is generally correlated with $Fe(CN)_6$ vacancy content. Specifically, when the crystal water content increases, the $Fe(CN)_6$ vacancy content also tends to rise. Furthermore, the simultaneous increase of these two factors typically corresponds to a decrease in Na^+ content. Behind these interrelated phenomena, complex principles of chemical equilibrium and crystal structure construction are involved.[46] In the structure of PBAs, M_A and M_B are connected by –CN– ligands, where the low-spin state is connected to C and the high-spin state is connected to N, which together form a complex three-dimensional framework structure (Fig. 2d).[47,48] This structure can endow PBAs with their characteristic large gap sites and ion transport channels. They have a unique size, shape and chemical environment that can accommodate Na^+, potassium ion (K^+) and other ions well.

According to the differences in $Fe(CN)_6$ vacancies, crystal water, and alkali metal ion content, the crystal structure of PBAs exhibit various phases, such as cubic phase, monoclinic phase, and rhombohedral phase.[49] The monoclinic and rhombohedral phases are both sodium-rich phases, with the key distinction lying in the presence or absence of interstitial water. The monoclinic phase contains interstitial water while the rhombohedral phase does not. Consequently, the monoclinic phase is regarded as the transition state between the cubic and rhombohedral phases. To exemplify, the Fe-based hexacyanoferrates (FeHCF) typically exhibit a cubic phase structure.[50,51] Nevertheless, alterations in the concentration of guest cations can intensify coulombic interactions with nitrogen atoms, potentially resulting in lattice expansion.[52] As observed in the case of sodium-rich FeHCF (Na_xFeHCF), when the sodium content exceeds 1.5, the asymmetric occupation of

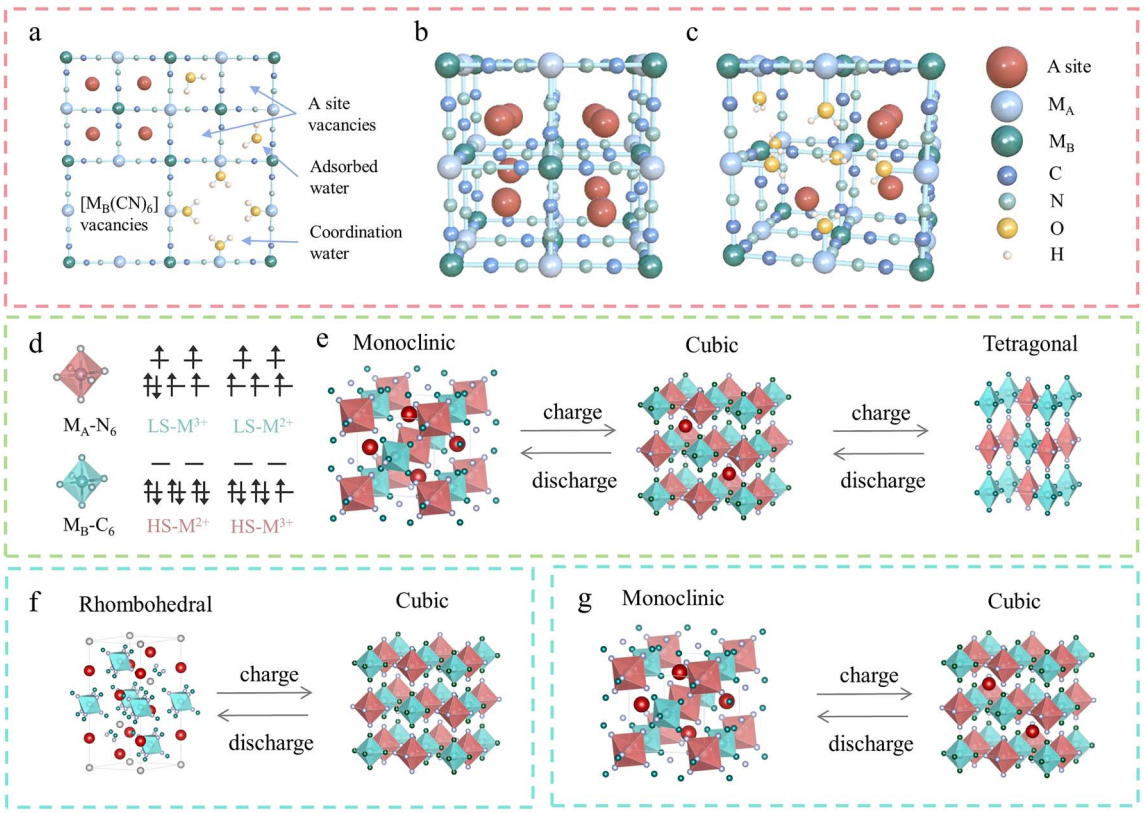

Fig. 2 (a) Cross-sectional view of PBAs containing crystal water and vacancies. (b) Framework structure of ideal PBAs. (c) Framework structure of PBAs with crystal water and vacancies. (d) Spin orbitals of M_A and M_B (HS denotes High Spin, LS denotes Low Spin). Electrochemical structural evolution of (e) monoclinic ↔ cubic ↔ tetragonal, (f) rhombohedral ↔ cubic and (g) monoclinic ↔ cubic.

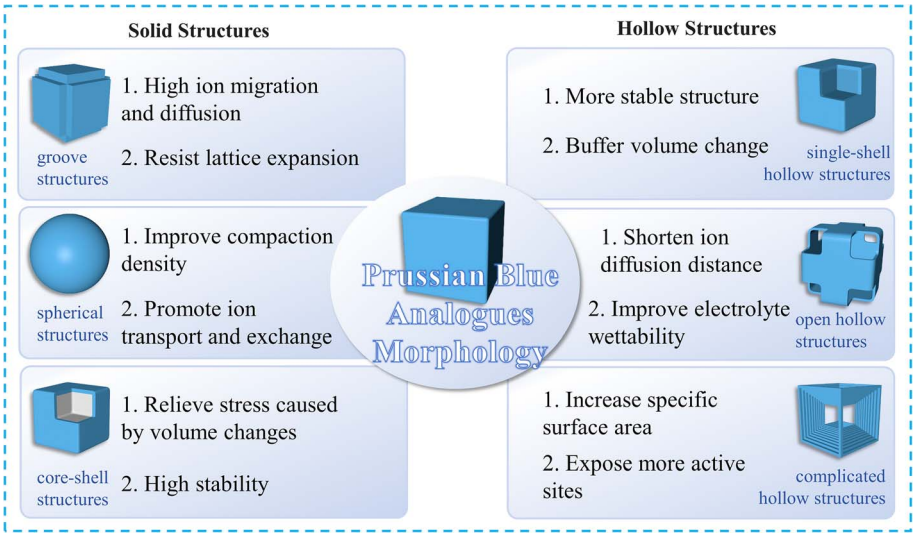

Fig. 3 Various morphologies of PBAs and their advantages.

electrons from transition metal ions in simple merged orbitals will have different electron shielding effects on the Na^+ in different directions, resulting in a phase transition from cubic to monoclinic phase.[53] Further removal of the crystal water will affect the distribution of the electron cloud, which reduces the Pauli repulsion in the framework, making the structure more susceptible to distortion. This contributes to the transformation of the material from the monoclinic into the rhombohedral phase, which is more distorted than the previous structure.

Phase transitions are also observed in electrochemical reaction processes. Specifically, when guest ions are reversibly inserted or extracted, manganese-based hexacyanoferrates (MnHCF) undergo a three-phase transition from the monoclinic to the cubic and then to the tetragonal phase (Fig. 2e). This transition is attributed to structural deformation of the Mn–N bond, particularly the octahedral deformation induced by Jahn–Teller distortion, which exhibits significant structural changes.[54,55] In contrast to MnHCF, FeHCF and cobalt-based hexacyanoferrates (CoHCF) typically exhibit a two-phase transition between the rhombohedral and cubic phases during the reversible insertion or extraction of guest ions (Fig. 2f).[53,56,57] Meanwhile, nickel-based hexacyanoferrate (NiHCF) and copper-based hexacyanoferrate (CuHCF) exhibit only minor deformation of the cubic crystal framework during electrochemical reactions (Fig. 2g). This behavior is associated with the electrochemical inertness of nickel and copper ion species.[58,59] Notably, the structural evolution of zinc-based hexacyanoferrates (ZnHCF) are strongly dependent on electrolyte concentration. In low-concentration electrolytes, ZnHCF transforms from the rhombohedral into the cubic phase, accompanied by enhanced solubility in aqueous solution.[60] However, in high concentrations of electrolyte, ZnHCF tends to maintain its rhombohedral structure without a phase transition.[61]

2.2 Morphology

The design of specific morphology plays a crucial role in improving the performance of PBAs, which are mainly classified into two categories: solid structures and hollow structures, each of which contains a variety of specific morphologies. Different morphologies will bring different advantages. For example, cubic structures have more active centers. Spherical structures have a more uniform particle size. Hollow structures have shorter ion diffusion and are more adaptable to volume changes, making them less prone to collapse (Fig. 3).

2.2.1 Solid structures. The solid structure can be classified into cubic, spherical, core–shell and other special morphologies. Cubic morphology is the typical morphology of PBAs, which can be prepared by a simple co-precipitation method and is also the common morphology in the laboratory.[62–64] It is worth noting that during the synthesis of cubic PBAs, the addition of chelating agents can slow down the growth of crystals and thus increase the crystallinity.[65] Meanwhile, the concentration of hydrogen ions also affects the morphology of the products. When the concentration of hydrogen ions is high, the nuclei are more likely to aggregate along the surface of the high-energy crystals thus producing a uniform cubic shape.[66] Etching treatment can improve its electrochemical properties, such as hydrochloric acid (HCl) etching and ammonia etching.[67,68] After the etching treatment, groove structures will be formed, which establish channels for ions to enter the interior, enhance the ability of ion migration and diffusion, and thus improve the performance of PBAs.

Spherical structures can be synthesized by a variety of methods, such as hydrothermal method, synthesis under polyvinyl pyrrolidone (PVP) assistance, *etc.*[69–71] The size and other properties of the resulting structures can be regulated by adjusting the reaction temperature and adding ethanol during the synthesis process. For example, a hydrothermal reaction temperature of 150–170 °C is suitable for the synthesis of nanospheres. Furthermore, the addition of ethanol can reduce the size of PBA nanoparticles, so that spherical PBAs with different sizes and properties can be customized to meet diversified application requirements.[72] The spherical structure of PBAs enhances micro-scale uniformity, leading to two

significant advantages. First, it improves the material's compaction density. Second, it facilitates better electrolyte penetration, thereby promoting ion transport and exchange.

In practical applications, PBAs with classical morphology frequently demonstrate accelerated capacity fading due to synergistic effects of structural degradation and parasitic side reactions. Therefore, products with special morphology can be designed and synthesized to solve these problems. One common morphology is the core–shell structure as a heterostructure, which consists of one or more materials as a shell structure around the main material.[73–75] Core-shell structures can be prepared in a variety of ways. A common method is to use an ion-exchange method to form a two-layer structure by taking advantage of the interactions between transition metal ions and specific ligands (*e.g.*, sodium citrate) and the differences in reaction kinetics during the preparation of PBAs.[76] Another method is to introduce a protective layer on the surface of PBAs through surface coating technology. Both methods can stabilize the interface of PBAs and improve their cycling stability.

2.2.2 Hollow structures. Hollow structures can be classified into three main categories: single-shell hollow structures, open hollow structures, and complex hollow structures. Among these, the single-shell hollow structure represents the most prevalent type of PBA hollow structure. This particular morphology offers significant advantages, including effective buffering of volume changes induced by Na^+ insertion/extraction, enhanced structural stability, and improved cycling performance.[77,78] The synthesis of single-shell hollow structures primarily involves two approaches: the etching method and the self-template method. The etching method involves the directional etching of materials using specific etchants to achieve the desired hollow structure.[79] For instance, the PVP-assisted HCl etching method can be employed to etch PBA particles in the presence of PVP, resulting in products with hollow structures. While this method is straightforward and convenient to implement, it presents notable drawbacks. Specifically, the HCl etching process can generate toxic hydrogen cyanide, posing potential risks to both environmental safety and experimental conditions. Alternatively, the self-template method represents another widely utilized synthesis strategy. This approach primarily relies on the use of precursors with specific shapes to construct hollow structures.[80] The precursor's material composition includes the ionic constituents necessary for the target product. During the reaction, the precursor gradually dissolves and releases the target ions by modulating the reaction environment (*e.g.*, pH, temperature), ultimately forming a single-shell hollow structure. In comparison to the etching method, the self-template method offers greater controllability and environmental friendliness. However, it typically entails a more complex synthesis process and imposes stricter requirements on precursor selection and reaction conditions.

Open hollow structures and complicated hollow structures are an extension of hollow structures. They present an internal hollow state and may form openings on the faces or frames of the cube, allowing the internal hollow portion to communicate with the external environment. The open hollow structure exhibits a shorter ion diffusion path, significantly enhancing the sodium ion migration rate.[81] This improvement facilitates better electrolyte permeability, ensuring sufficient contact between electrodes and electrolytes, thereby boosting the rate performance and reversible capacity of the materials. Additionally, complex hollow structures possess a larger specific surface area and a hierarchical pore structure, which provide more active sites and optimize ion and electron transport pathways. These special structures can overcome the performance limitations of traditional designs, showing promising potential in energy storage applications.[82,83] In summary, the morphology of PBAs is highly versatile and tunable. By employing various synthesis methods and modulation techniques, PBAs can be tailored to meet diverse application requirements.

2.3 Redox mechanism

Understanding the reaction mechanism of guest cations in the insertion/extraction process is crucial for the development of high-performance PBA electrode materials. According to the number of redox active sites involved in the reaction, PBAs can be classified into double electron transfer type (DE-PBA: M_A and M_B = Mn, Fe, Co) and single electron transfer type (SE-PBA: M_A = Zn, Ni and M_B = Fe, Co, Mn), and their theoretical specific capacities are 170 mA h g^{-1} and 85 mA h g^{-1}, respectively.[84] The two-electron transfer type has a high theoretical capacity and thus is promising and competitive for high energy density devices, even comparable to lithium iron phosphate, a well-known LIB cathode material (Fig. 4a). In contrast, single-electron transfer types have a stable structure and good conductivity properties during electrochemical processes, which makes them suitable for battery applications that require fast charging/discharging and long-term stable operation (Fig. 4b).[85] For a typical DE-PBA with ideal stoichiometry ($x = 2, y = 1$) and no crystal water interactions, the overall electrochemical equations controlling Na^+ insertion/extraction in the case of $Na_2Fe[Fe(CN)_6]$ can be described as follows:

Charge 1:

$$Na_2Fe^{II}Fe^{II}(CN)_6 \leftrightarrow NaFe^{III}Fe^{II}(CN)_6 + Na^+ + e^- \quad (2)$$

Charge 2:

$$NaFe^{III}Fe^{II}(CN)_6 \leftrightarrow Fe^{III}Fe^{III}(CN)_6 + Na^+ + e^- \quad (3)$$

Discharge 1:

$$Fe^{III}Fe^{III}(CN)_6 + Na^+ + e^- \leftrightarrow NaFe^{III}Fe^{II}(CN)_6 \quad (4)$$

Discharge 2:

$$NaFe^{III}Fe^{II}(CN)_6 + Na^+ + e^- \leftrightarrow Na_2Fe^{II}Fe^{II}(CN)_6 \quad (5)$$

For the charging process, at the beginning, Na^+ is extracted from the $Na_2Fe[Fe(CN)_6]$ lattice, and when the first Na^+ is completely extracted, Fe^{II} with high-spin coordinated to N is oxidized to Fe^{III} in order to maintain charge parity. The crystal structure begins to change from the initial high sodium content rhombohedral phase and the cell volume may begin to shrink

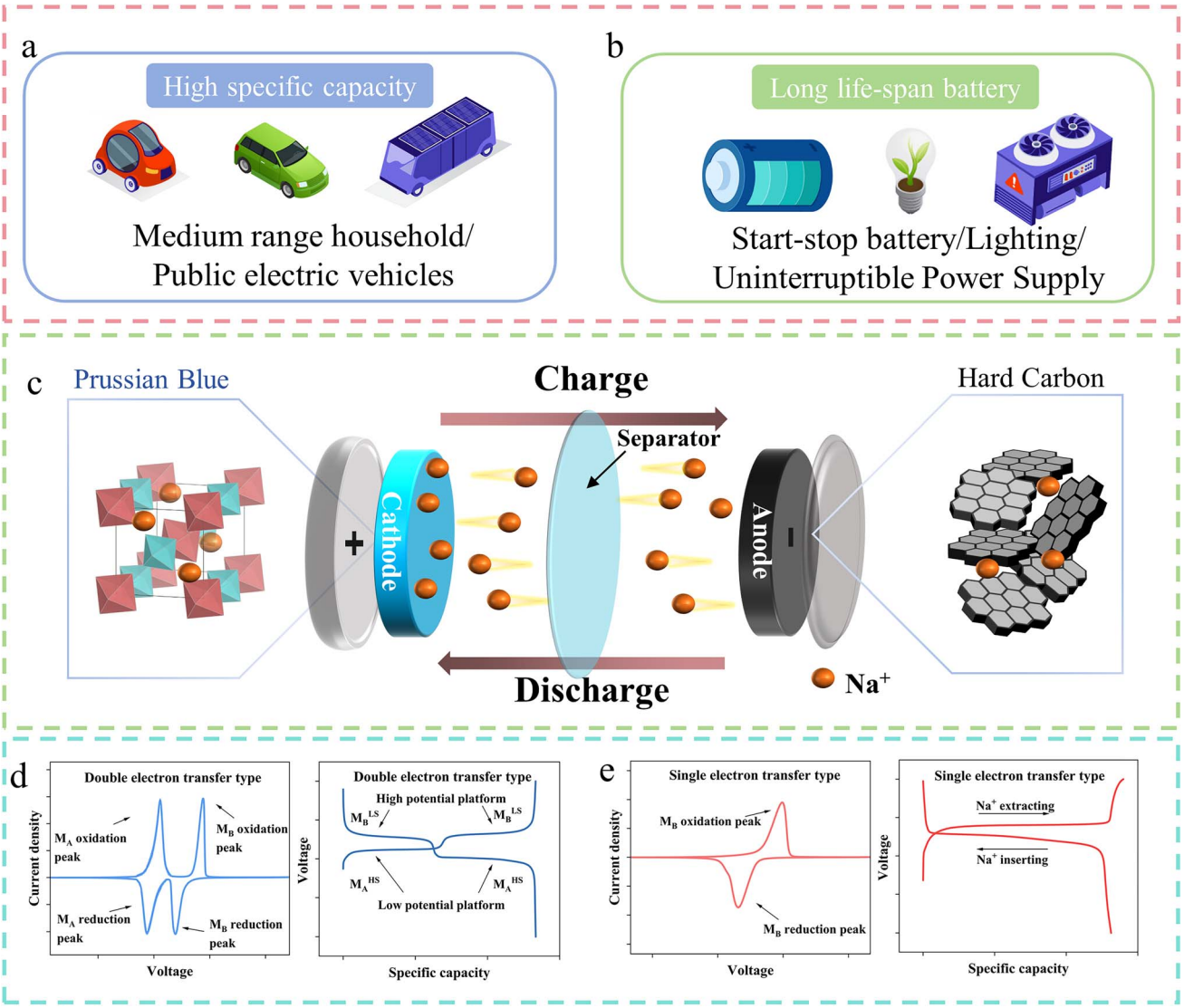

Fig. 4 (a) Application scenarios of double electron transfer type PBAs. (b) Application scenarios of single electron transfer type PBAs. (c) Schematic diagram of the SIBs (based on the PBA cathode and hard carbon anode). (d) Schematic diagram of CV and charge discharge curves for typical double electron transfer type. (e) Schematic diagram of CV and charge discharge curves for typical single electron transfer type.

slightly, corresponding to eqn (2). When the second Na^+ is extracted, the low-spin Fe^{II} coordinated to C is similarly oxidized to Fe^{III}. At this point the crystal structure reaches a relatively stable low-sodium or no-sodium state, which may show a cubic or other low-symmetry structure that is quite different from the high-sodium state, such as a smaller unit cell volume, corresponding to eqn (3) (Fig. 4c). The discharge process represents the reverse of the charging process. During this stage, Fe^{III} undergoes sequential reduction to Fe^{II}, accompanied by the gradual insertion of Na^+ into the crystal lattice. Concurrently, the crystal structure undergoes a series of transformations, transitioning from the low-sodium or sodium-free state back to the high-sodium rhombohedral phase. This structural restoration includes the recovery of key features, such as ion diffusion channels, to their initial configuration. These sequential processes complete the electrochemical cycle, as described by eqn (4) and (5). Corresponding to the two reaction platforms in the charge/discharge process described above, DE-PBA usually has two pairs of anodic/cathodic reaction peaks, while SE-PBA has one pair of anodic/cathodic reaction peaks. Fig. 4d and e respectively shows the cyclic voltammetry (CV) curves and charge discharge curves of typical double electron transfer type and single electron transfer type. However, it should be noted that not all DE-PBAs have two pairs of anodic/cathodic reaction peaks. For example, MnHCF has a high redox potential due to the strong ligand field of the low-spin Fe site coordinated to carbon, with a large 3d-orbital energy level splitting, and the electron filling of this site. In contrast, the high-spin Mn site is in a weaker ligand field, and the 3d-orbital energy level splitting is small, which results in the decrease of the redox potential of Mn. This ligand field difference leads to a comparable potential between the two, thus converging the

two possible redox peak pairs into one. However, the introduction of interstitial water molecules can weaken the ligand field, which may change the above equilibrium state and restore the two redox peaks.[86]

3 Challenges to the commercialization of PBAs

The commercialization of PBAs in SIB applications has achieved certain success. Fig. 5 shows the development of commercial products based on PBAs. In 2020, Natron Energy of the United States pioneered the commercialization of PBAs by launching the SIB BlueTray™ 4000, which utilizes PBA-based materials. This system exhibits a high-power utilization rate, occupies only half the footprint of lead–acid batteries, and achieves a rapid 0–99% state of charge within 8 minutes. These characteristics make it suitable for uninterruptible power supply in data centers, information technology/network cabinets, and other mission-critical industrial applications. This development marked the official entry of PBAs into commercial markets. In 2021, Contemporary Amperex Technology Co., Ltd of China launched its first-generation SIBs, addressing the capacity fading issue of Prussian White (PW) materials through innovative charge rearrangement technology. The cells demonstrate a specific energy of 160 W h kg^{-1}, achieving over 80% capacity after 15 minutes of charging at room temperature. Notably, the cells retain over 90% discharge capacity at −20 °C, with system integration efficiency exceeding 80%. Furthermore, the thermal stability of these cells significantly surpasses national safety standards. In 2022, Natron Energy expanded its product portfolio with the BlueRac™ 250 battery cabinet, which demonstrates remarkable performance characteristics. The system delivers a sustained discharge power of over 250 kW, enabling high-power applications. Additionally, it demonstrates exceptional fast-charging capabilities, reaching over 99% state of charge in just 15 minutes. Furthermore, the battery cabinet shows long cycle life, retaining over 90% capacity retention after 1000 cycles, making it suitable for high-utilization scenarios. This system is designed for grid storage, peak load regulation, load balancing, and mission-critical applications. In the same year, the Wenzhou University Technology Innovation Institute for Carbon Neutralization made a significant advancement in PBA technology by developing a specialized heat treatment method to effectively remove crystal water from PBAs. The innovative heat treatment process not only ensures the complete removal of crystal water but also maintains the structural integrity of PBAs, thereby enhancing their cycling stability and capacity retention. Leveraging this method, the institute achieved large-scale production of high-quality PBAs. In 2023, LI-FUN Technology of China, in collaboration with a number of companies, made the world's first PBA-based SIB storage system commercially available, further boosting the marketability of PBAs. In 2024, Zero One Four Adv. Mater. Co., Ltd of China achieved a significant breakthrough in SIB technology by developing and mass-producing 46-series full-tab large cylindrical SIBs. These batteries exhibit a remarkable capacity of 13.0 Ah and a high discharge rate of 15C, making them suitable for high-power applications. Notably, the cells demonstrate exceptional operational stability across an extreme temperature range of −50 to 80 °C, ensuring reliable performance in both frigid and high-temperature environments. This advancement not only highlights the company's innovative capabilities in battery design and manufacturing but also positions their products as a viable solution for demanding applications in renewable energy storage, electric vehicles, and industrial power systems. The successful commercialization of

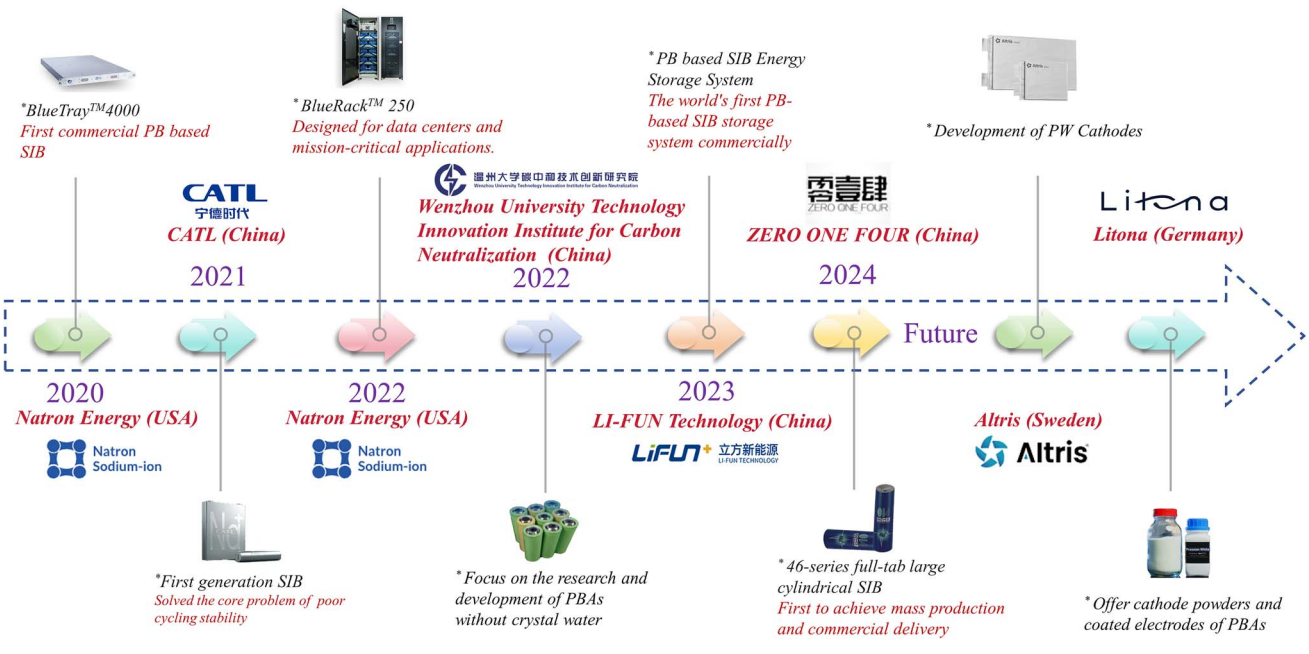

Fig. 5 Commercial product development based on PBAs.

these batteries marks a pivotal step forward in the development of next-generation energy storage technologies. With emerging companies such as Altris of Sweden and Litona of Germany joining the market, PBAs have a broader future in SIBs, which will provide more possibilities for renewable energy applications and power storage.

Despite their potential, several key issues remain in the future development of PBAs. These issues can be categorized as follows: crystal water, crystal defects, side reactions, transition metal dissolution, low conductivity, structural collapse due to the Jahn–Teller effect, and thermal runaway. Some of these challenges arise from the bulk phase, while others are associated with the interface. They affect stability, reduce electrochemical performance, and pose safety risks, all of which are critical factors hindering the commercialization of PBAs and warrant special attention.

3.1 Crystal water and crystal vacancies

Ideally, the synthesized PBAs should have a perfect crystal structure without any crystal water or vacancies. However, in practice, a simplified and accelerated co-precipitation reaction in aqueous solution is typically employed due to economic reasons. Given the negligible solubility product constant (K_{sp}) of PBAs in water, the nucleation and growth of grains proceed rapidly and simultaneously upon mixing of the precursor solutions. This process is accompanied by the formation of a large number of defects and vacancies, which are occupied by coordination and interstitial water. The presence of $Fe(CN)_6$ vacancies reduces the number of redox-active centers in the lattice, hindering the full activation of the Fe^{LS} redox reaction. This limitation directly reduces the Na^+ content and specific capacity of the material. Additionally, these vacancies compromise the structural integrity of the lattice, resulting in a distorted framework. Such distortion can lead to the breaking of chemical bonds during Na^+ insertion/extraction, potentially causing structural collapse over prolonged charge/discharge cycles, thereby significantly degrading the cycling stability of the battery.[87] Crystal water primarily resides in $Fe(CN)_6$ vacancies, while interstitial water, which is physically adsorbed on surfaces or interstitial lattice sites, can be relatively easily removed.[88–90] In contrast, coordination water forms strong bonds with Fe ions, altering the electronic states around Fe ions or $Fe(CN)_6$ groups, making its removal challenging. The presence of crystal water impedes Na^+ migration within the lattice, leading to reduced specific capacity and poor cycling stability. Furthermore, crystal water may undergo side reactions with the electrolyte during charge/discharge processes, compromising electrolyte stability. At high potentials, oxidative decomposition of crystal water can alter the electrochemical plateau, while interactions with material components can modify the crystal structure. These effects collectively deteriorate the sodium storage performance of PBAs.[91,92]

3.2 Side-reactions and thermal runaway

Safety is a non-negligible issue in the commercialization of electrode materials, and thermal runaway is the most dangerous safety issue for batteries. Although the theoretical oxygen-free structure of PBAs can avoid the common thermal runaway pathway associated with oxygen release, the introduction of crystal water is inevitable in practical applications, as we have already mentioned in the previous section. Therefore, it is important to clarify the side-reactions of PBAs in batteries and to analyze the potential thermal runaway. The current study points out that the side reaction generation of PBAs during charging and discharging is mainly divided into two stages.[93] Electrolyte decomposition at low potentials, such as organic carbonate electrolyte decomposition to produce C_2H_4 and C_2H_6, followed by the introduction of large amounts of interstitial water into the electrolyte. The reaction process is as follows:[94]

$$C_3H_4O_3 + Na^+ + e^- \rightarrow \frac{1}{2}(CH_2OCOONa)_2 + \frac{1}{2}C_2H_4\uparrow \quad (6)$$

$$C_2H_5OCOOC_2H_5 + Na^+ + e^- \rightarrow C_2H_5OCOONa + C_2H_5 \rightarrow C_2H_6\uparrow \quad (7)$$

At high potentials, the interstitial water at the anode undergoes a reduction reaction to produce H_2, and the electrolyte at the cathode is oxidized, catalytically opening the ring to produce CO_2. The reaction process is as follows:

$$H_2O/ROH + e^- \rightarrow OH^-/RO^- + \frac{1}{2}H_2\uparrow \quad (8)$$

$$C_3H_4O_3 + H_2O/OH^- \rightarrow C_2H_5O_2^- + CO_2\uparrow \quad (9)$$

The occurrence of side-reactions consumes the electrolyte on the one hand, causing degradation of battery performance. On the other hand, gas generation potentially causes battery expansion or even explosion.

In terms of thermal runaway, previous studies have indicated that PBAs display superior thermal safety characteristics. He *et al.*[95] evaluated the safety performance of the Natron battery, the first commercial sodium-ion pluggable battery using PBAs as the cathode. A short-circuit test found that the battery temperature returned to ambient levels within 6 minutes after increasing to 50–60 °C without any significant thermal runaway. However, Li *et al.*[96] found a hidden thermal runaway mechanism in PBAs, and crystal water is also the 'culprit' of this thermal runaway mechanism, which may cause internal hydrolysis and dismutation of PBAs. Although PBAs can maintain structural integrity below 200 °C, when the temperature rises to 325 °C, the M_A–N and M_B–C bonds will break, leading to significant release of cyanide groups and reaction with the electrolyte, resulting in a large amount of heat generation. Therefore, controlling defects and water content during the synthesis process is crucial for improving the overall safety of PBA cathodes. Overall, the exothermic behavior of PBA based SIBs has significantly improved compared to traditional LIBs, but it still needs to be considered as a key factor in large-scale applications.

3.3 Transition metal dissolution and structural collapse

PBAs face the problems of structural collapse due to the Jahn–Teller effect and the dissolution of transition metal ions during

the cycling process. MnHCF is posited as an exemplary cathode material, exhibiting a high capacity, high operating voltage of 3.5 V (*vs.* Na^+/Na), low raw material cost, and environmental friendliness.[23] A disadvantage of MnHCF is that Mn ions exist in different oxidation states. During the charging and discharging process, the electronic configuration of Mn ions may change, which can result in an uneven distribution of electrons in different orbitals. This phenomenon is known as the Jahn–Teller effect.[22,97] The Jahn–Teller effect results in the distortion of the crystal structure of MnHCF. Typically, the original cubic or tetragonal crystal structure undergoes deformation to a certain extent, and due to the inherent instability of the structure, the material is susceptible to collapse after numerous cycles. The pristine cubic or tetragonal crystal structures undergo certain degrees of distortion under repeated Na^+ insertion/extraction processes, primarily attributed to their inherent structural instability. This lattice distortion triggers irreversible phase transitions, accompanied by microstructural fractures and active material exfoliation. Concurrently, the dissolution of transition metal ions leads to the formation of electrochemically inert compounds, collectively exacerbating structural degradation and capacity deterioration.[98,99] During this process, the Mn–N_6 octahedra transition from a stable Mn^{2+} state to an unstable Mn^{3+} state. The resulting Mn^{3+} is then dissolved into the organic electrolyte through a disproportionation reaction:

$$2Mn^{3+} \rightarrow Mn^{2+} + Mn^{4+},$$

which leaves Mn vacancies on the surface.[23] Additionally, in the presence of trace water or elevated temperatures, the electrolyte or its decomposition products may interact with Mn ions, leading to further Mn depletion. This results in a reduction in active material, a decline in capacity and energy density, and a disruption of the structural integrity of the electrodes, causing chalking and shedding. Therefore, PBAs must overcome these critical challenges to achieve successful industrialization.

3.4 Low energy density and power density

Energy density and power density are key indicators for evaluating battery performance.[100] Energy density is the amount of electrical energy stored per unit volume or mass. In practical applications, higher energy density means higher gram capacity/volume capacity and miniaturization of battery volume. The China National Institute of Electronic Technology Standardization has released the '2023 Sodium-ion Battery Industry Research Report', which points out that the average energy density of China's sodium-ion battery industry is 104.1 W h kg^{-1}, with the highest being 129.2 W h kg^{-1} and the lowest 60 W h kg^{-1}, while the energy density of the current mainstream LIBs can reach 260–300 W h kg^{-1}.[101] It can be seen that there is still a considerable gap between SIBs and LIBs in terms of energy density. Power density characterizes the rate of energy output during discharge, which is related to the power performance and fast charging capability of the battery. Currently, some commercial PBA-based SIBs show a high power density (1250 W kg^{-1}), which is already higher than other batteries, including LIBs (usually <1000 W kg^{-1}), but still far from supercapacitors.[102]

For SIBs to be more competitive in the new energy market, they need to find ways to increase energy density and power density. According to the definitional formula of the two:[91]

$$E_d = \int_{V_s}^{V_e} Q \times V \, dv, \quad P_d = \int_{V_s}^{V_e} I \times V \, dv$$

We can find that to increase the energy density, the key is to increase the specific capacity and plateau voltage of the battery. The presence of crystal water in PBAs adversely affects their crystallinity, which we have described in detail in the previous section. In general, the presence of crystal water causes sodium loss, which affects the specific capacity of the material. Therefore, the amount of crystal water needs to be strictly controlled. At a certain specific capacity, increasing the plateau voltage can directly increase the energy density. For PBAs, the platform voltage can be increased by chemical modification or compounding of materials, for example, compounding with materials that have a high potential window, such as specific transition metal oxides or conductive polymers.[103] These additives can change the electrochemical environment of PBAs during the charging/discharging process, resulting in a positive shift of the redox potential, thereby increasing the overall plateau voltage. Power density is then related to current density and platform voltage. The ionic/electronic conductivity of the material directly determines the current density.[104] In PBAs, lower ionic/electronic conductivity restricts the rapid transport of ions and electrons inside the material, resulting in severe polarization and lower power density during high-current charging/discharging. To increase the ionic/electronic conductivity, several strategies can be used. A common approach in commercial applications is to compound with highly conductive materials such as carbon nanotubes or graphene.[105,106] These materials are able to build a continuous conductive network in the PBA matrix, which not only provides a fast transport channel for electrons, but also promotes ion migration through synergistic effects. Increasing the specific surface area of PBAs enhances the contact between the electrode and the electrolyte, promoting the rapid adsorption and desorption of ions, which is crucial for improving power density. A straightforward approach to increasing the specific surface area is to reduce the particle size of the material. However, it is important to note that excessively small particles may lead to agglomeration, resulting in poor dispersion. Another effective approach involves enhancing the electrode compaction density, which is intrinsically linked to the tapped density of the active material.[107] When the compaction density of the electrode increases, the amount of active material relatively was increased accordingly under the same battery volume, thereby improving the energy density of the battery. At the same time, it can realize the thinner electrode under high mass loading conditions. This structural advantage facilitates the preservation of continuous electrical pathways and efficient ionic transport during cycling.[108]

3.5 Engineering challenges

While intrinsic material defects (*e.g.*, crystal water and vacancies) fundamentally limit the electrochemical performance of PBAs, engineering challenges in large-scale manufacturing pose equally critical barriers to commercialization. Transforming laboratory-scale synthesis into industrial production requires addressing critical issues such as electrode slurry processing. The hygroscopic nature of PBAs complicates slurry preparation under ambient humidity, where residual crystal water or adsorbed moisture reacts with polar solvents in conventional slurry systems, leading to slurry viscosity instability and inhomogeneous particle dispersion.[88,109] Furthermore, PBAs synthesized *via* rapid co-precipitation methods typically exhibit irregular morphologies and broad particle size distribution – issues exacerbated during scale-up. Agglomerated particles disrupt the rheological properties of slurries, resulting in coating defects during electrode fabrication. These issues collectively hinder the uniformity and reproducibility of large-format electrodes, underscoring the necessity for process innovations tailored to PBAs' unique physicochemical characteristics.

4 Bulk phase regulation for PBAs

Bulk phase regulation is a core strategy for optimizing the performance of PBAs as cathode materials in SIBs. Its significance lies in addressing key challenges faced by PBAs in practical applications, such as low specific capacity, poor cycling stability, and low operating voltage, by accurately modifying the lattice/composition inside the material. By regulating the bulk phase, the crystal structure, electronic properties, and ion transport kinetics of PBAs can be finely tuned, significantly enhancing their electrochemical performance (Fig. 6).

4.1 Heat treatment and the use of chelating agents

Since the discovery of the potential of PBAs as cathode materials, crystal water and crystal defects have remained as key issues, and they are also the biggest obstacles to the commercialization of PBAs. Currently, researchers have devised a number of methods to obtain PBAs with high crystallinity and minimal crystal water by carefully optimizing various synthetic conditions. These include adding chelating agents, adjusting the solution pH, thermal treatment, and employing advanced synthesis techniques.

Heat treatment of synthesized PBAs is a simple and efficient method to remove crystal water. Theoretically, the crystal water in PBAs can be completely removed at around 220 °C, which can be obtained by thermogravimetry analysis (TGA). However, it should be noted that rough heating by high temperature may damage the structure of the material and lead to the deterioration of its electrochemical properties. Therefore, the appropriate treatment temperature and gentle treatment need to be further explored. Wang *et al.*[49] heat-treated the material at 270 °

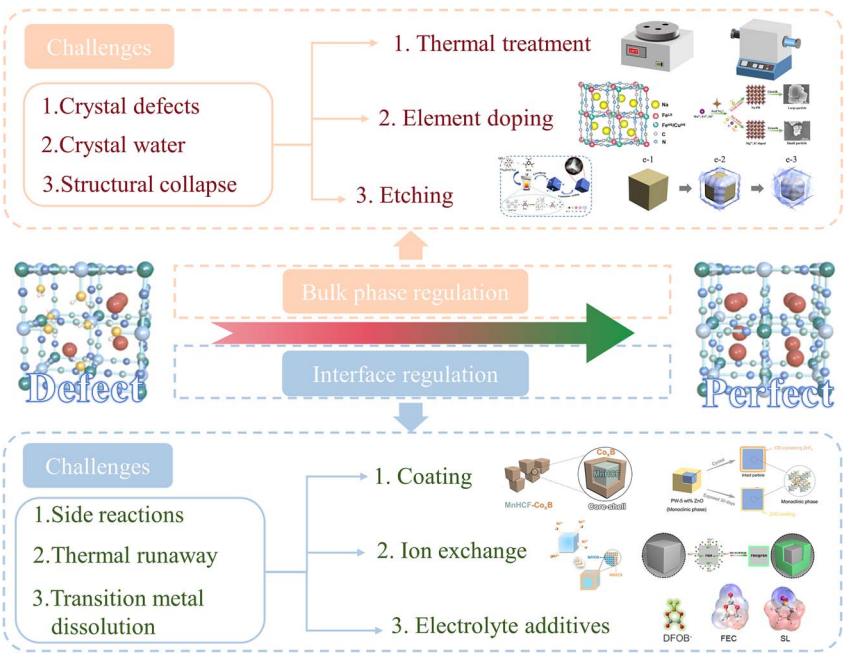

Fig. 6 Issues and countermeasures in the commercialization process of PBAs. All insets are from the literature. Reproduced with permission from ref. 110 Copyright 2022, American Chemical Society. Reproduced with permission from ref. 111 Copyright 2024, Wiley-VCH. Reproduced with permission from ref. 112 Copyright 2024, American Chemical Society. Reproduced with permission from ref. 113 Copyright 2017, American Chemical Society. Reproduced with permission from ref. 114 Copyright 2023, Wiley-VCH. Reproduced with permission from ref. 115 Copyright 2024, American Chemical Society. Reproduced with permission from ref. 116 Copyright 2021, Springer Nature. Reproduced with permission from ref. 117 Copyright 2021, Elsevier. Reproduced with permission from ref. 118 Copyright 2024, Wiley-VCH. Reproduced with permission from ref. 119 Copyright 2024, American Chemical Society.

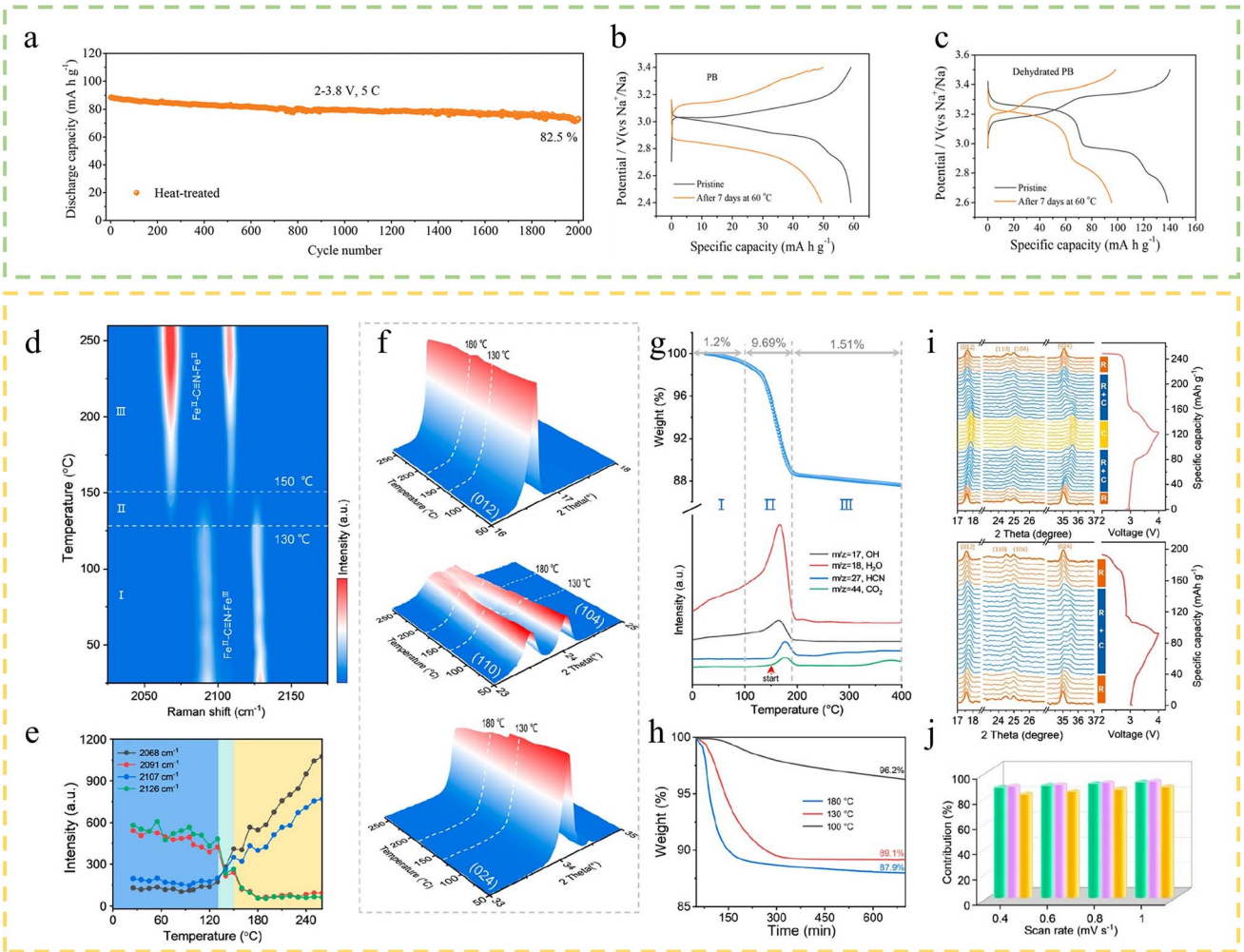

Fig. 7 (a) Cycling performance of HT sample at the current density of 5C. (b and c) Capacity storage performance of the pristine and dehydrated PB after 7 days at 60 °C.[49] Copyright 2022 Wiley-VCH. (d) The contour plots and (e) the normalized intensity of four peaks corresponding to *in situ* H-Raman. (f) *In situ* H-XRD patterns. (g) TG-MS curves. (h) Thermostatic TG curves at 100, 130, and 180 °C. (i) *In situ* XRD spectra of PB and PB-130. (j) The capacitive contribution ratio.[120] Copyright 2024, American Chemical Society.

C under argon protection, which almost completely eliminated the crystal water inside the material. The heat-treated material has excellent cycling stability performance (82.5% capacity retention for 2000 cycles at 5C), while the high-temperature capacity storage performance of the material has been significantly improved (Fig. 7a–c). In addition, Ge *et al.*[120] applied the appropriate dehydration temperature of PB by various online monitoring techniques. *In situ* heating Raman spectroscopy (*in situ* H-Raman) revealed that the near-surface structure of PB remained stable between 25 and 130 °C. Upon heating to 130–150 °C the weak peaks at 2068 and 2107 cm^{-1} intensified, while the strong peaks at 2091 and 2126 cm^{-1} weakened and eventually disappeared, indicating the reduction of Fe^{III} under thermodynamic stress. Beyond 150 °C, the PB structure underwent continuous degradation (Fig. 7d and e). *In situ* heating X-ray diffraction (*in situ* H-XRD) further confirmed that the (110)/(104) diffraction peaks began to weaken at 130 °C and merged at 180 °C, signaling the onset of structural collapse (Fig. 7f). Thermogravimetric-mass spectrometer technique (TG-MS) analysis showed that the weight loss between 25 and 100 °C was attributed to the removal of adsorbed water, while the significant weight loss at 130 °C corresponded to the elimination of a substantial amount of crystalline water, during which the PB structure remained intact (Fig. 7g). Thermostatic thermogravimetric experiments demonstrated that after maintaining temperatures at 100 °C, 130 °C, and 180 °C for 12 hours, the removal rates of crystalline water were 3.8%, 10.9%, and 12.1%, respectively (Fig. 7h). *In situ* X-ray diffraction (*in situ* XRD) analysis reveals that the PB heated at 130 °C (PB-130) undergoes a reversible structural transition from rhombohedral to quasi-cubic phase during charging, while the presence of interstitial water in the PB sample results in a mixed-phase state of rhombohedral and cubic phases, limiting its electrochemical activity (Fig. 7i). Additionally, it provides structural support to vacancies, enhancing the cycling stability of the material (Fig. 7j). The results demonstrate that retaining a trace amount of coordination water not only improves the material's kinetics

but also alters the coordination environment of Fe^{LS}, extending the high-potential plateau.

Introducing chelating agents to control the crystallinity and crystal water content of PBAs is a common regulatory method. Chelating agents can form stable complexes with metal ions, interfere with normal crystal growth during the crystallization process, slow down nucleation rate, promote ordered growth of crystal nuclei, and improve crystallinity. At the same time, the complex will change the solution chemical environment, so that the original and water molecules closely bound to the metal ions by the chelating agent. Water molecules detach from the coordination structure and become free, making them easier to remove. Jiang *et al.*[121] successfully prepared low-defect Prussian blue (LD-PB) using sodium carboxymethylcellulose (CMC) as the chelating agent. The binding energy of different chelating agents with Fe^{3+} was calculated by density functional theory (DFT), and it was found that the binding energy of CMC was moderate, which could improve the crystallinity of PB. The rate performance of LD-PB is excellent, with good capacity and retention at current densities from 0.5 to 100C (101 mA h g^{-1} at 100C), and 97.4% capacity retention after 3000 cycles. Wang *et al.*[122] employed ethylenediaminetetraacetic acid disodium (Na_2EDTA) as a chelating agent and ascorbic acid (VC) as a pH regulator to synthesize poly-PBAs. The 'acid effect' of VC regulates the chelating ability of the chelating agent with transition metals and reduces the transition metal vacancies to synthesize PBAs with high crystallinity (*e.g.*, EDTA-1MVC). X-ray diffraction (XRD) showed that EDTA-1MVC is a sodium-rich rhombohedral phase with a crystallinity of 94.7%, which is higher than that of the comparative sample, sodium citrate-1M VC (Nacit-1MVC) (65.97%) (Fig. 8a and b). TGA showed a reduction in the water content of EDTA-1MVC, which was 14.28% (the comparative sample was 17.10%) (Fig. 8c). Charge/discharge tests showed that EDTA-1MVC exhibited excellent performance at different current densities, *e.g.*, a discharge capacity of 82.0 mA h g^{-1} at 6 A g^{-1}, and a good cycling stability (86.32% capacity retention after 10 000 cycles at 6 A g^{-1}) (Fig. 8d and e).

Previous views equated defects with bottom performance, but recent studies have shown that appropriate defects unexpectedly contribute to the performance enhancement of PBAs. Shang *et al.*[123] achieved a significant breakthrough in the field of PBAs by successfully introducing manganese vacancies (V_{Mn}) into $Na_2Mn[Fe(CN)_6]$ (NMF). Through the utilization of Na_2-EDTA as a strong chelating agent, they synthesized a novel compound, $Na_{1.6}Mn_{0.75}(\square Mn)_{0.25}[Fe(CN)_6]\cdot 1.57H_2O$ (EDTA-NMF) (Fig. 8f and g). This pioneering work marked the first successful construction of non-conventional cationic vacancies in PBAs, opening new possibilities for material design and optimization in this field. Electron spin resonance (ESR) spectroscopy confirmed the increase of V_{Mn} (Fig. 8h). The introduction of V_{Mn} suppressed Mn–N bonding, which significantly mitigated the Jahn–Teller aberration during the cycling process. It was shown that the initial capacity could go up to 137 mA h g^{-1} at a current density of 25 mA g^{-1}. And the capacity retention rate was as high as 72.3% after 2700 cycles at a current density of 500 mA g^{-1} (Fig. 8i). Besides, Liu *et al.*[30] improved the capacity and cycling stability of PBAs by introducing a synergistic strategy of Fe vacancy and Cu doping. It was shown that Fe vacancy and Cu doping improved the Na^+ diffusion kinetics and increased the specific surface area of the material, as well as stabilized the structure of the material. These methods of controlling the defect content provide new ways to improve the performance of PBAs. In addition, there are some other methods to control the vacancies by improving the synthesis method that are also feasible for practical applications. For example, Wan *et al.*[124] proposed a post-synthesis and *in situ* vacancy repair strategy to synthesize high-quality FeHCF in a high-concentration $Na_4Fe(CN)_6$ solution, and this *in situ* repair method can repair vacancies from the inside out and activate the reduction reaction at the 24d site.

4.2 Elemental doping

The doping and substitution of ions take advantage of the adjustable structure and composition of PBAs, by using various transition metals (TMs) or alkali metals (AMs) for doping in PBAs, thus exerting the synergistic effect between various elements.[125]

4.2.1 Transition metal site doping. In the development of practical electrode materials for PBAs, TM sites offer a large number of alternatives. Due to their mixed valence nature and open three-dimensional backbone structure, PBAs can be chemically modified without disrupting the overall crystal structure. When substitution at TM sites occurs, their geometry typically remains unchanged. The lattice parameters and channel sizes are linearly related to the ionic radius of the cation at the TM sites, while the reactive potential of the anionic sites is influenced by the ionic potentials (charge to radius ratios) of the TM, leading to higher insertion potentials.[126] This effect is attributed to increased σ-bond polarization and more pronounced π-back bonding in cyanide ligands, as well as the lower energy of the t_{2g} orbitals on the R-site ions.[127] The regulation method of using various TMs to dope each other and exert their respective characteristics can effectively regulate the redox behavior and electronic/ionic properties of PBAs, thereby improving their electrochemical performance.[128]

Suitable doping elements can be selected through DFT calculations. Li *et al.*[26] compared the performance of different doping elements through DFT calculations. They employed the integrated crystal orbital Hamilton population (ICOHP) function to assess the strength of the chemical bond of N–transition metals (N–TM). Among a series of ICOHP values for N–TM (TM = Mn, Fe, Co, Ni, Cu, Zn), the Cu–N bond has the lowest ICOHP value, followed by Zn–N. Although Zn–N also demonstrated a relatively low ICOHP value, Cu is preferred due to its redox activity, which contributes to enhanced electrochemical performance. Density of states (DOS) calculations demonstrated that Cu doping decreased the bandgap from 2.37 eV to 0.65 eV, thereby improving electronic conductivity. Furthermore, diffusion barrier analysis revealed lower energy barriers in K-based monoclinic structures compared to Na-based cubic frameworks, indicating enhanced Na^+ transport kinetics in the K-stabilized configuration. These findings highlight the potential of Cu substitution in stabilizing the structure of PBAs and

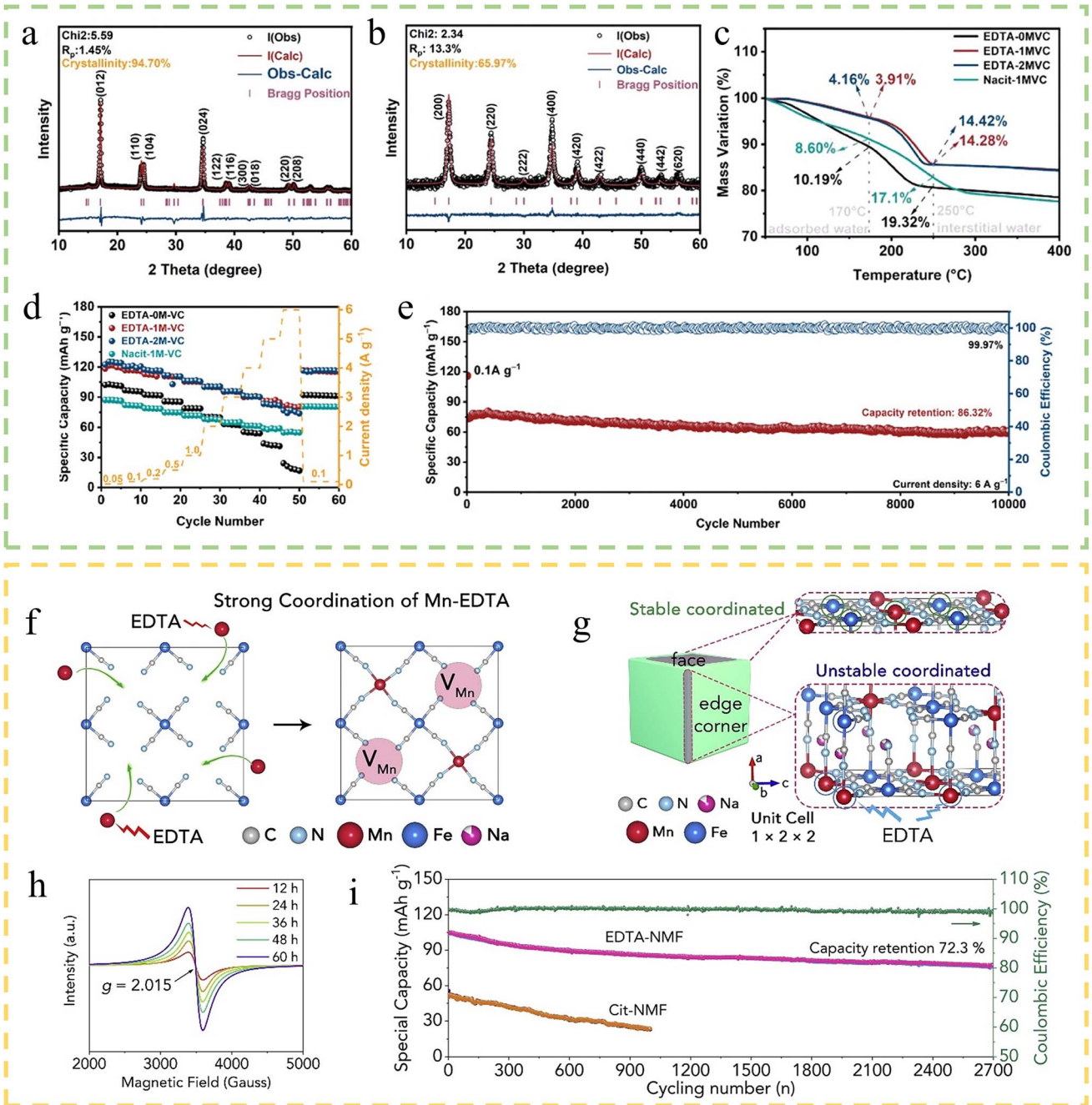

Fig. 8 (a) Rietveld refinement XRD pattern of EDTA-1MVC (b) Nacit-1MVC. (c) TGA comparison curve in N_2. (d) Rate performance of all the cathodes. (e) Long-term cycling performance of EDTA-1MVC at 6 A g^{-1} after 10 cycles at 0.1 A g^{-1}.[122] Copyright 2024, Wiley-VCH. (f) The formation mechanism of Mn vacancies in NMF. (g) Etching mechanism of NMF with Na_2EDTA. (h) ESR spectra of EDTA-NMF obtained at different reaction times. (i) Cycling performances of two NMFs at 500 mA g^{-1} and the coulombic efficiency of hexapod EDTA-NMF.[123] Copyright 2020, Elsevier.

improving their functional properties. Chen *et al.*[110] directly synthesized Cu-doped FeHCF (Cu–FeHCF) by the co-precipitation method. It was shown that Cu doping significantly improved the activity of Fe^{LS}, and Cu played an important role in stabilizing the structure of FeHCF in the process of Na^+ insertion/extraction (Fig. 9a). Cu–FeHCF exhibits an initial capacity of 127.4 mA h g^{-1} at 100 mA g^{-1}, and the capacity retention rate was high and the decay rate was low after 500 cycles at 2 A g^{-1} (Fig. 9b). Zhang *et al.*[129] investigated the effect of Zn substitution on the sodium storage performance of Fe-based Prussian blue (Fe-PB), and they confirmed that Zn substitution could reduce the energy barrier and band gap of Fe-PB by DFT calculations (Fig. 9c–e). CV and galvanostatic charge/discharge tests showed that the increase in the capacity of Zn-substituted Fe-PB composite (FeZn-PB) originated from the increase in the activeness of Fe^{LS} and Fe^{HS}, and that the

contribution of the capacity of Fe^{LS} was significantly increased by Zn substitution. Besides, the results of electrochemical impedance spectroscopy (EIS) and galvanostatic intermittent titration technique (GITT) further confirmed that Zn substitution improved the diffusion kinetics of Na^+. It is shown that FeZn-PB exhibits excellent electrochemical performance, with an initial discharge capacity of up to 145.0 mA h g^{-1} at 20 mA g^{-1}, and an impressive capacity after 500 cycles at 1 A g^{-1}. In addition, Zhang *et al.*[130] introduced Zn to replace high-spin Fe in Fe–PBAs (ZnFeHCF) to control the depth of charge and discharge, leading to a highly reversible phase transition process and improving cycling stability. By studying the structural evolution of ZnFeHCF during charge and discharge processes using *in situ* XRD and *in situ* Raman spectroscopy (*in situ* Raman), it was found that it undergoes a reversible two-phase transformation (cubic phase and tetragonal phase), with small volume changes and good structural reversibility, which is the reason for its excellent cycling stability.

Due to the 'zero strain' characteristic of Ni during the insertion/extraction process of sodium, its doping promotes excellent structural stability of the lattice, often used to enhance the cycling stability of MnHCF, FeHCF, *etc.*[132] Peng *et al.*[131] synthesized Ni substituted $Na_2Mn_{0.5}Ni_{0.5}[Fe(CN)_6]$ (MNHCF-3) using an improved chelating agent assisted co-precipitation method at room temperature, which exhibited excellent electrochemical performance in SIBs, such as a capacity retention

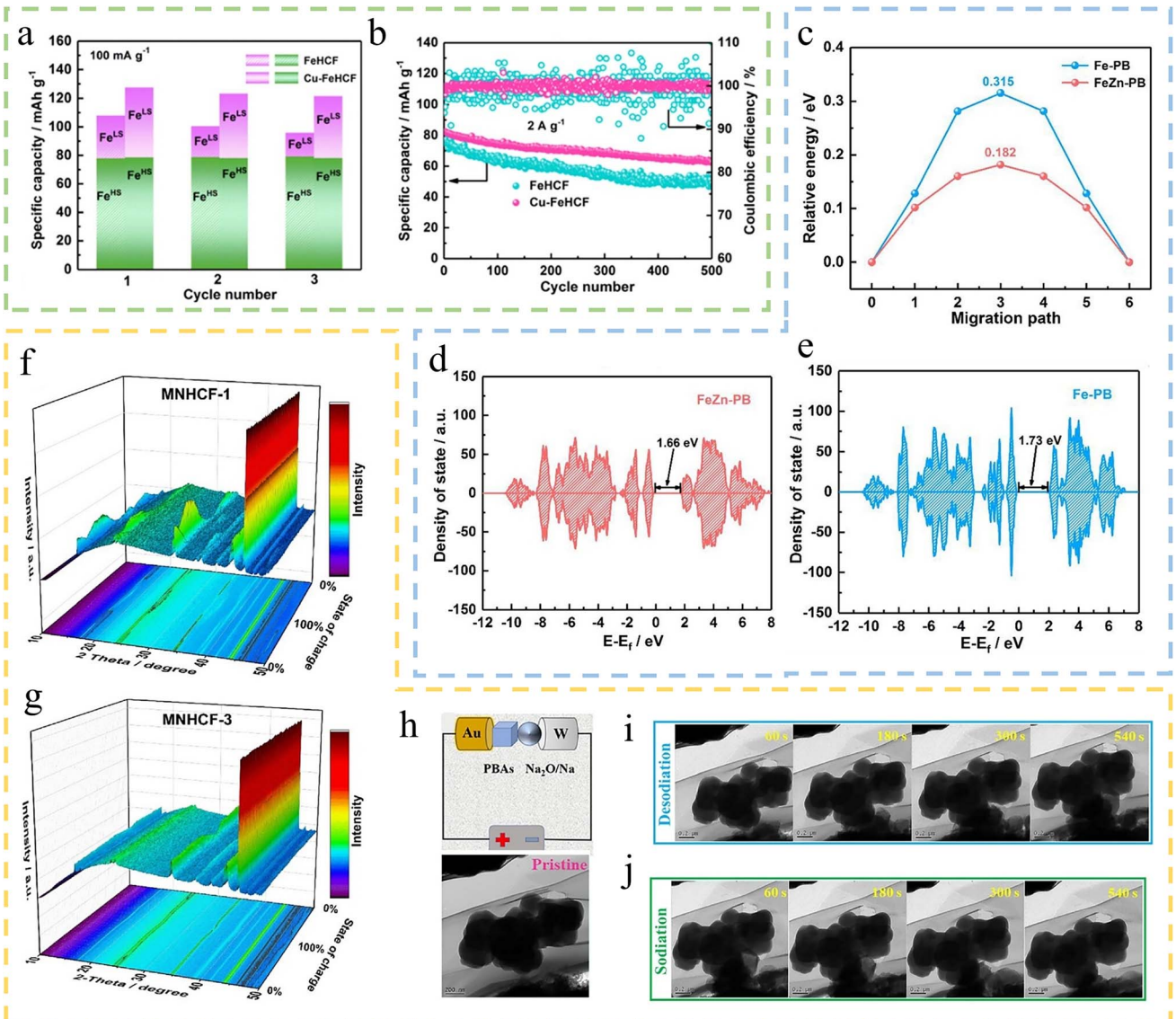

Fig. 9 (a) First three charge–discharge corresponding capacity contribution diagrams of Fe^{LS} and Fe^{HS} of FeHCF and Cu–FeHCF at 100 mA g^{-1}, respectively. (b) Long cycle performance of FeHCF and Cu–FeHCF at 2 A g^{-1}.[110] Copyright 2022, American Chemical Society. (c) The energy barrier profiles of Fe-PB and FeZn-PB, and (d and e) of Fe-PB and FeZn-PB, respectively.[129] Copyright 2021, Elsevier. (f and g) *In situ* PXRD 3D colormap surface with projection of MNHCF-1 and MNHCF-3. (h) Schematic illustration of *in situ* TEM setup and image of pristine particles of MNHCF-3. (i and j) Sequential images of MNHCF-3 from *in situ* TEM measurements during desodiation and sodiation processes.[131] Copyright 2024, American Chemical Society.

rate of 88.5% at 3000 mA g^{-1}, a capacity retention rate of 90.1% after 10 000 cycles, good climate stability from −10 to 60 °C, and excellent cycling stability of the entire battery. They revealed the mechanism of its excellent performance through *in situ* powder XRD (*in situ* PXRD) and *in situ* Transmission Electron Microscopy (*in situ* TEM). *In situ* PXRD analysis revealed that $Na_2Mn_1[Fe(CN)_6]$ (MNHCF-1) undergoes a phase transition from monoclinic to cubic and eventually to tetragonal during charging due to Na^+ extraction, while MNHCF-3 exhibits high reversibility during the cycling process, with a narrow angular offset, and can return to its original position with strong intensity during the reverse process (Fig. 9f and g). *In situ* TEM observations demonstrated the structural stability of MNHCF-3, with negligible volume shrinkage (2.3%) during desodiation and reversible volume recovery during sodiation (Fig. 9h–j).

In summary, by designing the ion doping and substitution strategies of TM sites, the structure of PBAs can be effectively optimized to enhance their performance in SIBs, including the improvement of the conductivity of the electrode materials, the rate of Na^+ migration, as well as the cycling stability and specific capacity of the materials.

4.2.2 Alkali metal site doping. Doping at AM sites is a crucial strategy for optimizing the crystal structure of PBAs. PBAs feature a large cavity structure with numerous interstitial sites (*e.g.*, 8c, 24d, 32f, and 48g) capable of accommodating AM cations or water molecules.[133] However, the non-stoichiometric occupation of these cations and the resultant low degree of filling within the cavities can introduce substantial amounts of interstitial water, leading to cell expansion. This expansion adversely affects the initial coulombic efficiency and cycling stability of the battery.[134] Modulating AM sites by introducing different metal ions can alleviate these issues by altering electron density and inducing lattice shrinkage.[98] Besides, the ionic radius of inserted metal ions significantly influences the insertion process. Thermodynamically, the radius of the inserted ion determines the free energy of the insertion reaction. As the ion size increases, the most stable gap within the structure shifts from face-centered to body-centered. DFT calculations indicate that larger insertion ions, due to stronger steric interactions, result in higher reaction potentials, thereby enhancing energy density. This phenomenon has been experimentally validated in compounds like CuHCF, NiHCF, and ZnHCF.[135,136] Nevertheless, larger cations exhibit slower migration rates, and excessively large cation radii can cause significant structural distortions, degrading cycling performance. Therefore, selecting an optimal cation size is essential to balance thermodynamic and kinetic properties for achieving superior material performance.[134,137]

There have been many studies related to AM doping, but considering the cost factor and feasibility, we mainly discuss the element K below.[138–140] The larger ionic radius of K^+ expands the backbone of PBAs, acting as a structural "pillar", thus enlarging the cell volume for Na^+ intercalation and enhancing specific capacity and cycling stability. A balanced mix of K^+ and Na^+ ions not only enlarges the sodium storage space but also maintains the stability of the PBA framework. Additionally, K^+ promotes the formation of a cubic structure with high crystallinity, which is crucial for maintaining structural integrity during the charge and discharge processes, especially at high rates.[141] Zhang *et al.*[142] developed a potassium-assisted iron-based PBA (NKPB-3) with low defect and water content by carefully designing the crystal structure and crystal phase orientation. It was shown that the introduction of K^+ changes the crystal orientation, reduces $[Fe(CN)_6]^{4-}$ vacancies and crystal water content. *In situ* Raman and *in situ* XRD have demonstrated that the changes in NKPB-3 during cycling are highly reversible (Fig. 10a and b). Fig. 10c shows the schematic diagram of NKPB-3 phase transition mechanism. NKPB-3 shows outstanding electrochemical performance with an initial specific capacity of up to 147.9 mA h g^{-1} and an energy density of 450 W h kg^{-1}, which make it comparable to commercial $LiFePO_4$ battery materials. In addition, NKPB-3 demonstrated 83.5% capacity retention after 300 cycles over a long period of time (Fig. 10d). Gao *et al.*[141] synthesized $Na_{2-x}FeMn[Fe(CN)_6]$ (FeMnPBA) and 3% K-doped FeMnPBA (K-FeMnPBA3) using sodium citrate as the chelating agent (Fig. 10e). The initial discharge capacity of K-FeMnPBA3 was higher than that of FeMnPBA (139.1 mA h g^{-1}), and it also possessed a higher energy density (446.8 W h kg^{-1}). The EIS results indicated that moderate K^+ doping promotes Na^+ diffusion, but over doping hinders diffusion by occupying Na^+ storage sites (Fig. 10f). Meanwhile, they successfully synthesized K-FeMnPBA3 at the kilogram level in a 50 L reactor (Fig. 10g). The initial discharge capacity of the pouch battery assembled using K-FeMnPBA3 as the cathode and Kuraray hard carbon as the anode was 114.3 mA h g^{-1}, and the capacity retention rate was 82.6% after 600 cycles at 1C, which has the potential for practical application (Fig. 10h–j).

In addition, Xu *et al.*[111] utilized low-grade water (*e.g.*, seawater) to synthesize PB, enabling natural ion doping (*e.g.*, Mg, K) and achieving low-cost, sustainable preparation. They employed a chelator-assisted co-precipitation method to synthesize PB materials (DW-PB, LW-PB, SW-PB, and TW-PB) using deionized water, lake water, sea water, and tap water, respectively. Among these, SW-PB exhibited superior electrochemical performance, delivering a discharge capacity of 115.8 mA h g^{-1} at 0.1C and a capacity retention rate of 93.9% after 500 cycles at 5C. Meanwhile, they proposed a purification strategy for separating impurity ions from wastewater by precipitation and ion exchange, and the recovered sodium citrate and Na_2SO_4 were of high purity; this recycling strategy can significantly reduce the average raw material cost, which provides a good idea for the commercialization of PBAs.

Compared with the general TM site regulation, the research on AM site regulation provides more opportunities for the development of new cathode materials for SIBs to improve the performance. At present, the regulation of AM sites in PBAs is still a complex and challenging field. Further study of these ions may provide more insight into the development of new ESSs.

4.2.3 Anion site doping. In addition to cation doping, regulating the anionic sites of PBAs is also an important means to improve material properties. This approach involves restructuring the coordination chemistry environment of the material, enabling precise design of both crystal structure and

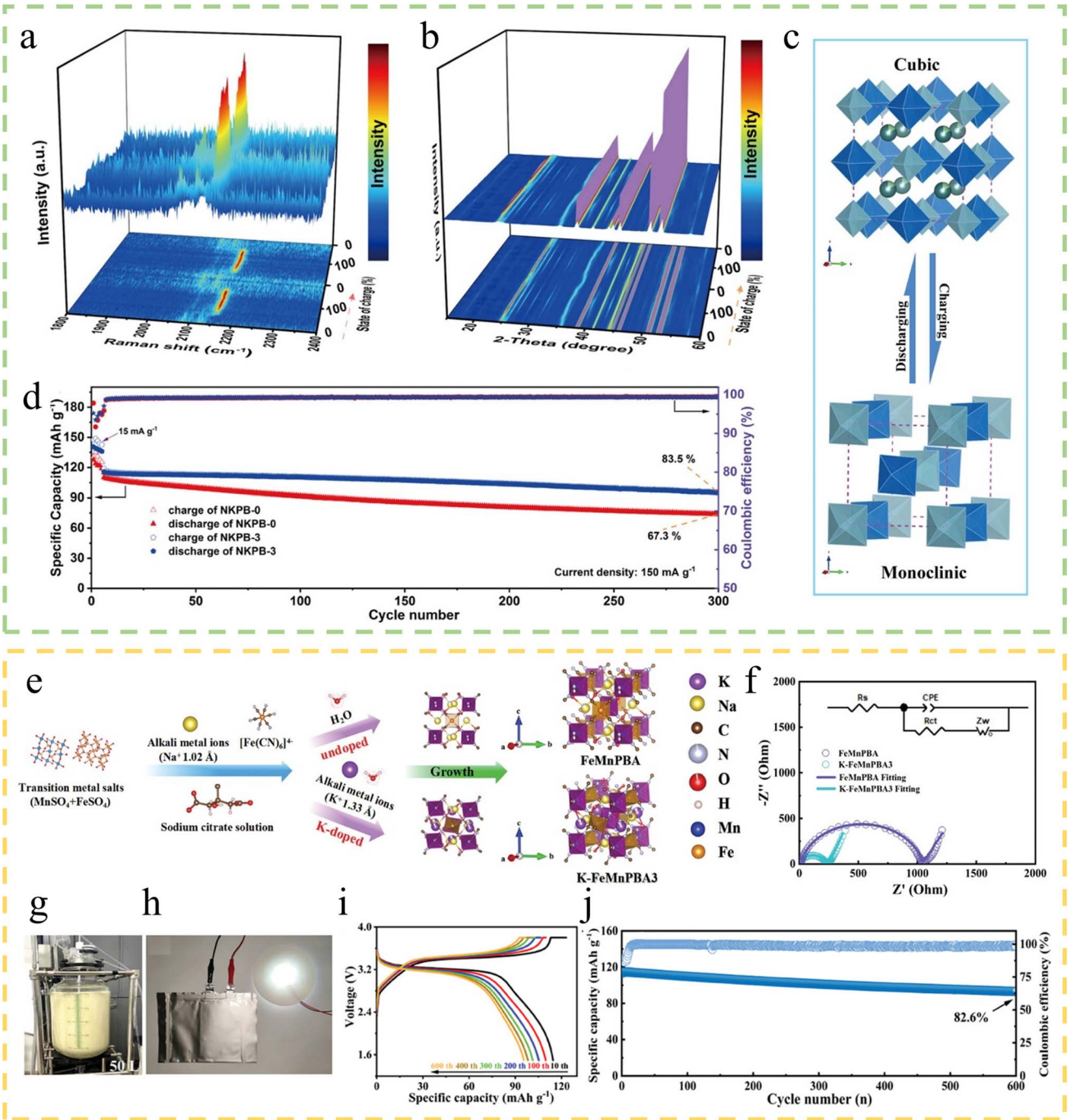

Fig. 10 (a) *In situ* Raman 3D colormap surface with projection. (b) *In situ* XRD 3D colormap surface with projection. (c) Schematic illustration of the phase transition mechanisms of NKPB-3. (d) Cycling performance of NKPB-3.[142] Copyright 2023, Wiley-VCH. (e) Schematic illustration of the synthesis process of as-prepared samples. (f) EIS spectra and fitting data. (g) Large-scale synthesis in kilogram scale of K-FeMnPBA3 (50 L). (h) Assembling of the pouch cell. (i) The charge–discharge curves of different cycles of the pouch cell. (j) Cycling performance of the pouch cell.[141] Copyright 2024, Wiley-VCH.

electronic properties. The underlying mechanism stems from the intrinsic influence of anionic groups on the transition metal coordination network: introducing anions with distinct coordination capabilities alters their bonding modes with transition metals (*e.g.*, Fe, Mn), thereby synergistically optimizing lattice symmetry, electron cloud distribution, and Na^+ diffusion pathways.[143] Lee *et al.*[144] synthesized manganese hexacyanomanganate ($Na_2Mn[Mn(CN)_6]$, denoted as MnHCMn) as a cathode material for SIBs through substitution of $Fe^{II}(CN)_6$ with $Mn^{II}(CN)_6$. The obtained MnHCMn exhibits a monoclinic structure featuring nonlinear Mn–N and C–Mn bonding configurations, along with eight large interstitial sites occupied

by Na^+. As shown in Fig. 11a, electrochemical analysis demonstrates that there were three distinct Na^+ insertion stages during cycling, delivering a reversible capacity of 209 mA h g^{-1}. Han *et al.*[145] obtained highly stable manganese nitrosylpentacyanoferrate ($Mn[Fe(CN)_5NO]$) by introducing nitroso groups (N═O) to replace some cyanide groups at the anionic site of MnHCF. This anionic engineering approach reduced the lattice water content and suppressed volume fluctuation during cycling *via* an octahedral spatial rotation mechanism (Fig. 11b–d). DFT calculations revealed that $Mn[Fe(CN)_5NO]$ exhibits lower binding energy with lattice water on its (111)/(110)/(100) crystalline surfaces compared to MnHCF, indicating reduced water adsorption. The N═O bond suppresses lattice water formation during synthesis, lowering material hydration and enhancing cycling stability, ultimately achieving 82.1% capacity retention after 400 cycles at 100 mA g^{-1} (Fig. 11e). The introduction of specific anionic groups can adjust the water adsorption energy within the lattice framework, effectively reducing non-active lattice water occupation at sodium storage sites. At the same time, this optimization can enhance intrinsic capacity and cycling stability by preserving active sodium accommodation positions. Such an anionic engineering strategy provides atomic-level design flexibility for constructing high-performance PBA electrodes, which transcends the conventional limitations of performance enhancement through sole reliance on cationic substitution.

4.3 Etching

Etching is an important method used to modulate the structure and properties of PBAs, which can generally be performed using

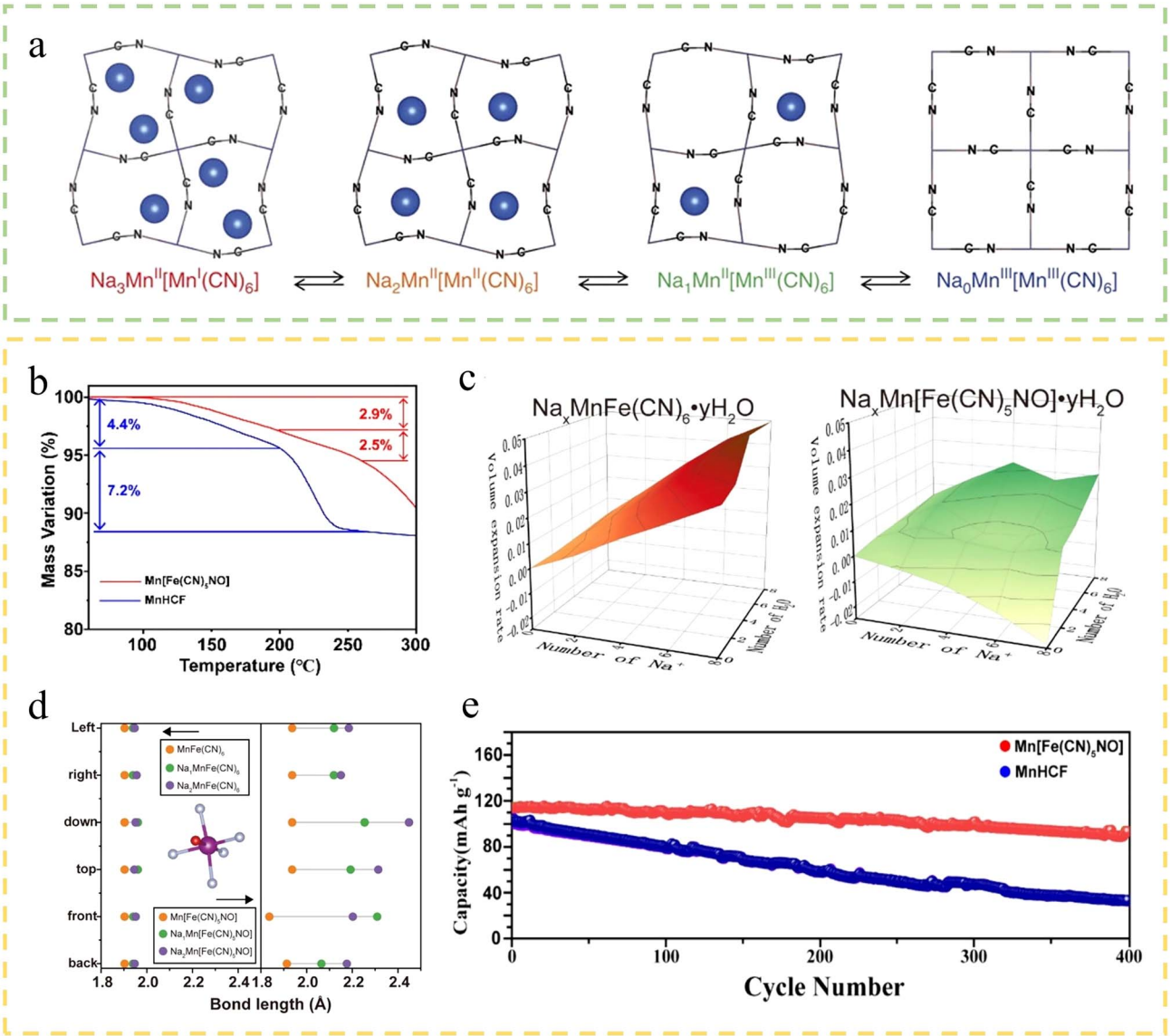

Fig. 11 (a) The schematic diagrams illustrate the changes in structure for MnHCMn during battery cycling.[144] Copyright 2014, Springer Nature. (b) TG curves of $Mn[Fe(CN)_5NO]$ and MnHCF. (c) Volume change of a unit cell with different water contents during Na^+ insertion of $Na_xMnFe(CN)_6$ and $Na_xMn[Fe(CN)_5NO]$. (d) Variation of manganese bond lengths with different sodium contents. (e) Cycle performance of $Mn[Fe(CN)_5NO]$ and MnHCF at a current density of 100 mA g^{-1}.[145] Copyright 2024, Elsevier.

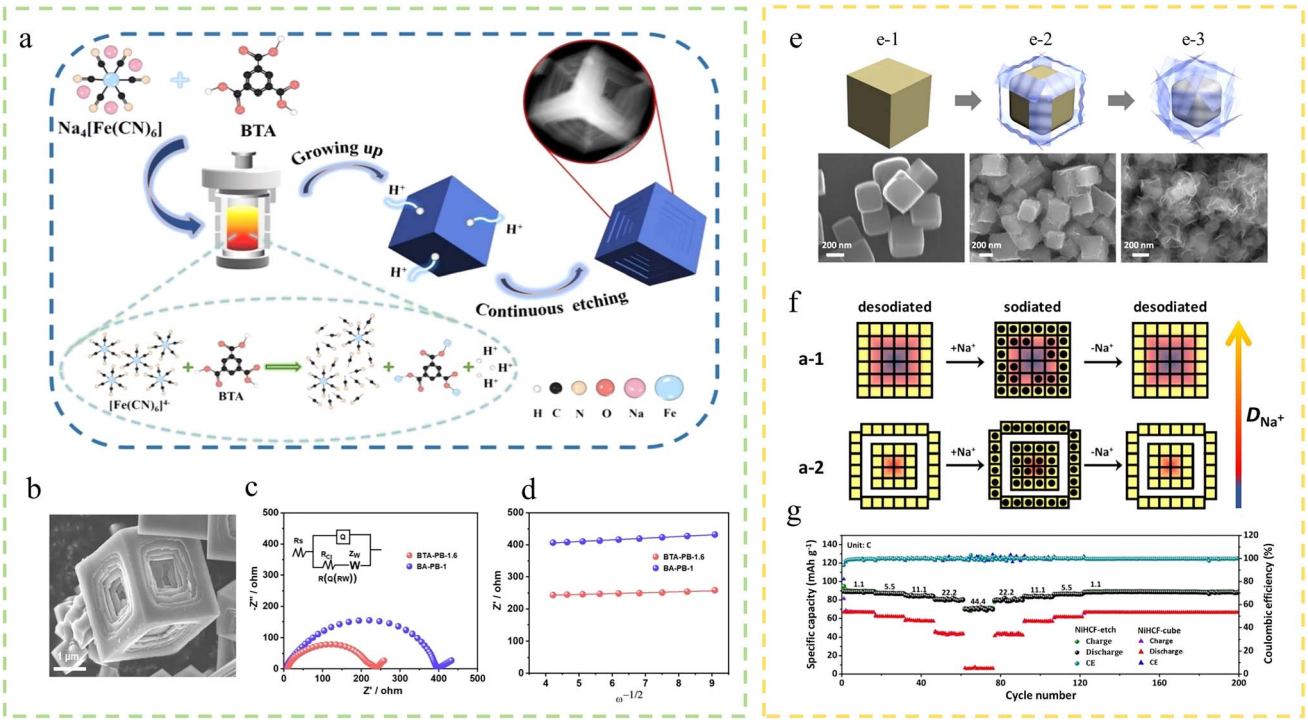

Fig. 12 (a) Scheme of the synthesis process of BTA-PB. (b) SEM images of BTA-PB-1.6. (c) EIS spectra of BTA-PB-1.6 and BA-PB-1. (d) Corresponding relationship between Z' and $\omega^{-1/2}$.[112] Copyright 2024, American Chemical Society. (e) Schematic diagrams accompanied by FESEM images of the NiHCF products after the etching time for (e-1) 0 hours, (e-2) 0.5 hours, (e-3) 6 hours. (f) Outside–in diffusion route of Na in NiHCF-cube and NiHCF-etch. (g) Rate performance of NiHCF-cube and NiHCF-etch.[113] Copyright 2017, American Chemical Society.

acid solutions such as hydrochloric acid or organic reagents such as tannic acid (TA). The principle of etching to form specialized structures is based on breaking the coordination bonds within the PBA framework to produce TM ions and $[Fe(CN)_6]^{4-}$ ions. The resulting disordered structural domains or defects manifest themselves in a heterogeneous manner within metal–organic frameworks or coordination polymer crystals (even single crystals).[146] Defects such as ligands, amorphous portions and dangling bonds in polycrystal domains are readily generated during non-classical crystallization processes. Heterogeneous distribution of defects inside PBA crystals induces inhomogeneous etching kinetics depending on the local concentration of the defects. For instance, the rate of etching will be greater in regions exhibiting a higher density of defects. It has been previously reported that the planar stability of PBAs is lower than that of corners or edges. As a result, the middle of the outer surface of the cube can dissolve faster during etching, resulting in a nanoframe-like morphology. The microstructure of PBAs can be precisely modified through etching techniques, such as transformation from solid structures into spherical, hollow, or other morphologies, thereby enhancing the material's specific surface area. Such structural changes provide more channels and active sites for the embedding and detachment of ions, which is conducive to improving the electrochemical performance of the material in applications such as batteries. Zhao *et al.*[68] modulated the $Na_2NiFe(CN)_6$ morphology through ammonia etching for 3 hours and obtained corner-passivated dice-shaped PBAs (NaNiHCF-3). NaNiHCF-3 showed good cycling stability (94% retention after 1000 cycles at 1C). The *in situ* XRD showed that the excellent cycling performance was due to the special structure that suppressed the phase transition during charging/discharging. Meanwhile, they calculated that the Na^+ in NaNiHCF-3 has shorter diffusion paths and lower spreading energy barriers (0.11 eV) by the climbing image-nudged elastic-band method, resulting in good reaction kinetics. Wang *et al.*[112] used 1,3,5-benzene tricarboxylic acid (BTA) as the etchant to synthesize a hollow layered Fe-PB cathode material (BTA-PB-1.6) by the hydrothermal method (Fig. 12a). For comparison, they employed benzoic acid (BA) as a substitute for BTA to synthesize BA-PB composites (BA-PB-1), alongside Fe-PB prepared *via* a coprecipitation method. The SEM image displays its hollow layered structure (Fig. 12b). The hollow layered structure mitigates the lattice volume changes induced by the Na^+ insertion/extraction process and maintains the integrity of the crystal structure after cycling. Therefore, it exhibits good cycling performance (80% retention after 200 cycles at 1C). Meanwhile, EIS indicates that BTA-PB-1.6 (233.9 Ω) has a lower R_{ct} than BA-PB-1 (394.5 Ω). The results indicate that the hollow layered structure shortens the diffusion path of Na^+ and increases the Na^+ diffusion coefficient of the material (Fig. 12c and d). In addition, Mai *et al.*[113] prepared etched NiHCF (NiHCF-etch) through a two-step process, starting with the coprecipitation synthesis of NiHCF-cube (NiHCF-cube) followed by an alkaline corrosion process. The morphological evolution at various etching stages was captured using Field-emission scanning

electron microscopy (FESEM), as depicted in Fig. 12e. Their findings underscore that Na^+ diffusion in NiHCF electrodes predominantly follows an outside–in pathway, with Na^+ mobility being the critical determinant of reaction efficacy (Fig. 12 f). Specifically, in NiHCF-cube, the extended diffusion pathways for Na^+ lead to insufficient utilization of reaction centers in the core region. Conversely, the NiHCF-etch variant markedly diminishes this diffusion length. Such architectural refinement ensures comprehensive accessibility to reaction sites, thereby optimizing the utilization of the central zone and augmenting the electrode's overall functionality. The surface-activated NiHCF-etch cathode, achieved through preferential etching, demonstrates exceptional rate performance with a specific capacity of 71.0 mA h g^{-1} at 44.4C, making it a highly promising candidate for long-lasting, high-power SIBs (Fig. 12 g).

Evidently, the etching method typically enhances the specific surface area of the material, shortens the Na^+ diffusion path, and enhances its diffusion kinetics, effectively addressing the poor ionic/electronic conductivity of PBAs, and thus is worthy of in-depth investigation.

5 Interface regulation for PBAs

After obtaining high-quality PBAs with low crystal water and crystal defects through bulk phase regulation, the influence of the interface on the material gradually dominated.[147] The interface issues of PBAs can be divided into surface issues and electrolyte interface issues. Metal ions on the surface of PBAs have limited chemical stability in the electrolyte and can dissolve from the material surface. The dissolution of surface metal ions and the depletion of the electrolyte deteriorate the interface, ultimately leading to electrode failure. At the same time, during the cycling process, PBAs react with the electrolyte, leading to the formation of a cathode–electrolyte interface (CEI) film. An excessively thick CEI film hinders ion transport and exacerbates polarization.[148] Therefore, regulating the interface to control these factors is crucial for constructing high-performance PBAs.

5.1 Surface coating

In nature, many soft and fragile objects possess protective shells on their surfaces, a feature that has evolved to counteract external threats. For surfaces exposed to such threats, applying a protective layer is a logical solution, this approach is known as surface coating technology. Surface coatings offer a straightforward method to address interface-related issues. By applying various materials as a physical barrier on the surface of PBAs, they have the following functions. First, they isolate the material from direct contact with external elements such as electrolytes, air, and water. Second, they help mitigate the material's volume expansion during cycling. Additionally, if the coating materials selected have superior electrical conductivity compared to the PBAs themselves, such as carbon or conductive polymers, they can enhance the overall electrical conductivity. This improvement, in turn, boosts the material's electrochemical performance. Certain coatings, such as conductive polymer coatings, effectively suppress the dissolution of TM ions.[85] The nitrogen and sulfur-containing heteroatoms in these polymers (*e.g.*, pyrrolic N in polypyrrole, imine N in polyaniline, and thiophene S in PEDOT) form strong coordination bonds with TM ions, substantially increasing the energy barrier for TM ion detachment from the lattice.[149] This enhanced chemical anchoring inhibits ion migration. Additionally, the dense coating layer acts as a physical barrier, isolating the PBA surface from direct electrolyte contact, thereby reducing the solvation erosion of TM ions by H_2O/H^+. Concurrently, it buffers the interfacial pH to suppress Mn^{3+} disproportionation reactions. Xu *et al.*[114] constructed a Co_xB coating layer on the surface of MnHCF by a simple room temperature chemical wet coating method. TEM and energy dispersive X-ray spectroscopy (EDS) confirmed the successful introduction of the Co_xB coating layer (Fig. 13a). The Co_xB coating effectively inhibited the dissolution of Mn between MnHCF and the dielectric, and buffered the volume change of MnHCF during charging and discharging (Fig. 13b). The MnHCF modified with 5 mol% Co_xB (MnHCF-5%Co_xB) exhibited excellent cycling stability (81% capacity retention after 450 cycles at 1C and 74% capacity retention after 2500 cycles at 10C) (Fig. 13c). Fu *et al.*[150] successfully constructed a conductive polymer perylene tetracarboxylic dianhydride (PTCA) coating on the surface of Fe-PB. Compared with Fe-PB (3.406 $m^2 g^{-1}$), PTCA-coated Fe-PB (Fe-PB@PTCA) (13.654 $m^2 g^{-1}$) has a larger specific surface area (Fig. 13d). EIS indicates that the R_{ct} of Fe-PB@PTCA decreased from 353.8 Ω to 285.7 Ω, and it has higher Na^+ diffusion coefficient (D_{Na^+}) than Fe-PB. The first discharge capacity of Fe-PB@PTCA is 145.2 mA h g^{-1} at 100 mA g^{-1}, and 73.4% capacity retention after 1000 cycles at 1 A g^{-1} current density (Fig. 13e and f).

In addition. Zhang *et al.*[115] constructed ZnO coating on the surface of PW with the aim of improving the air stability of PW. X-ray photoelectron spectroscopy (XPS) and TGA showed that the ZnO coating reduced the formation of surface hydroxyls, Fe–O compounds, sodium loss and PW decomposition in humid air. The soaking experiments further confirmed that the PW modified with 5 wt% ZnO (PW-5 wt%@ZnO-E) surface had fewer degradation products. The ZnO coating improves the cycling performance of PW by promoting the formation of ZnF_2-rich CEI, maintaining structural stability, reducing the generation of microcracks, and isolating the effects of humid air (PW-5 wt% ZnO: 91.5% capacity retention after 200 cycles at 0.3C. PW: 65.5% capacity retention after 200 cycles at 0.3C.) and air stability.

5.2 Ion exchange

Ion exchange, as a commonly used modification, is the use of cations or anions to transform a material into something else with the help of solid–liquid reactions, depending on the solubility of the candidate material.[151] For example, the highly soluble $Na_{2-x}MnFe(CN)_6$ ($K_{sp} \approx 8 \times 10^{-13}$ molar per L) can be converted to the less soluble HCF by ion exchange. With the ion exchange process, a special structure is formed in which a high specific capacity core component is combined with

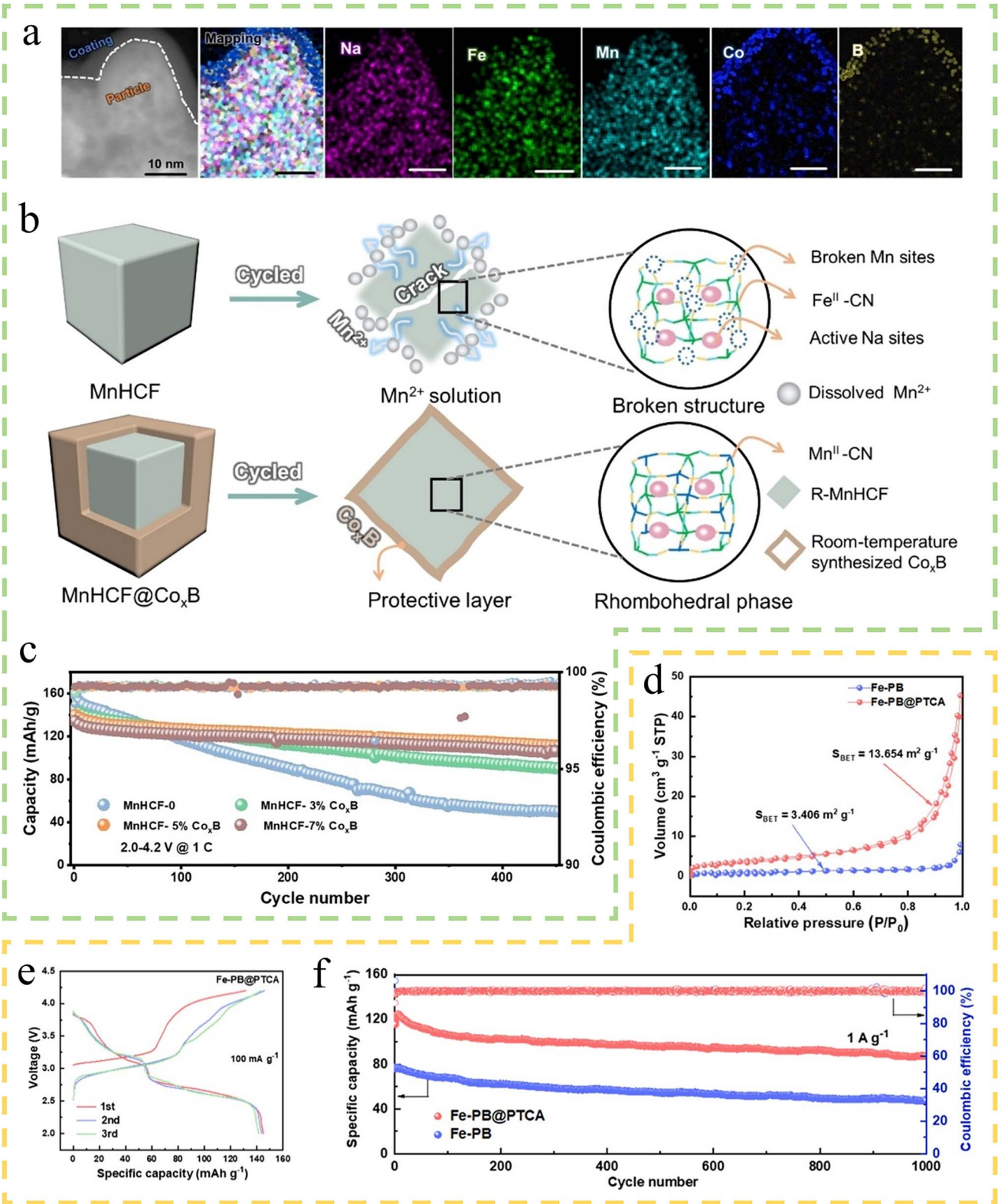

Fig. 13 (a) TEM and EDS element mapping of MnHCF-5%Co_xB. (b) Schematic illustration of the proposed protective mechanism of Co_xB to suppress the Mn dissolution and generation of microcracks of the MnHCF cathode. (c) The cycling stability of several electrodes at 1C.[114] Copyright 2023, Wiley-VCH. (d) N_2 adsorption–desorption isotherms of Fe-PB and Fe-PB@PTCA. (e) Charge/discharge profiles of Fe-PB@PTCA at 100 mA g^{-1}. (f) Long cycle performance of two samples at 1 A g^{-1}.[150] Copyright 2024, Wiley-VCH.

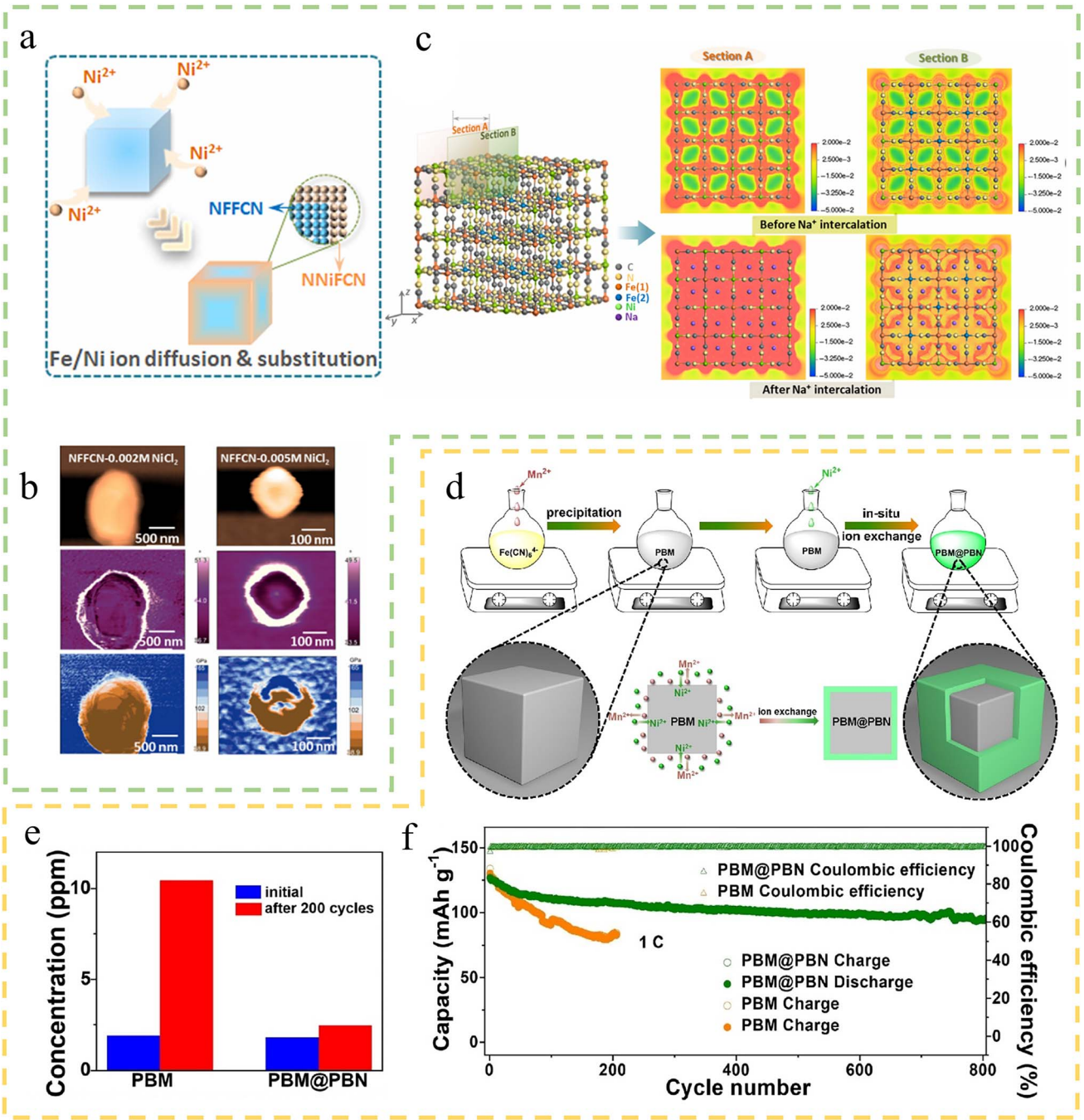

Fig. 14 (a) Schematic illustrating the preparation of core–shell NNiFCN/NFFCN. (b) AFM topography images, phase images, and stiffness tomography images of NFFCN-0.002 M $NiCl_2$ and NFFCN-0.005 M $NiCl_2$ (from up to down). (c) Electrostatic potential of NFFCN before and after Na^+ intercalation.[116] Copyright 2021, Springer Nature. (d) Schematic illustration of the synthesis process of the PBM@PBN sample. (e) Measurement of Mn dissolution in the electrolyte after a long-term cycle. (f) Cycling performance of PBM@PBN and PBM at 1C.[117] Copyright 2021, Elsevier.

a structurally stable outer surface, which contributes to the construction of a stable EEI and thus improves cathode stability. Cheng *et al.*[152] prepared high-performance sodium manganese hexacyanoferrate (MnFe-PB) coated with sodium copper hexacyanoferrate (CuFe-PB) (MnFe-PB@CuFe-PB) by the ion exchange method through the introduction of Cu element, which is a low-cost raw material and environmentally friendly. The CuFe-PB coating improved the structural stability of the material, inhibited the dissolution of Mn, and had a very good protective effect on the material. Meanwhile, XRD and XPS confirmed that the CuFe-PB coating did not change the structure and elements of MnFe-PB. Sun *et al.*[116] synthesized a core–shell structure of nickel hexacyanoferrate (NNiFCN) coated with iron hexacyanoferrate (NFFCN) (NNiFCN/NFFCN) using an *in situ* solvent-thermal method (Fig. 14a). Multifrequency atomic force microscopy (MAFM) proves that when using NNiFCN as

the outer shell, stress is generated in the NFFCN core (Fig. 14b). Meanwhile, the DFT calculation results indicate that a built-in electric field is induced in the NNiFCN/NFFCN framework, which facilitates Na^+ diffusion and leads to a higher Na^+ diffusion coefficient (Fig. 14c).

In addition, Feng *et al.*[117] synthesized sodium manganese hexacyanoferrate coated by sodium nickel hexacyanoferrate (PBM@PBN) electrodes by solution precipitation and *in situ* ion exchange (Fig. 14d). Inductively coupled plasma mass spectrometry analysis demonstrates that the PBN coating effectively suppresses Mn ion dissolution, thereby enhancing the cycling stability of the material. As a result, the PBM@PBN composite exhibits outstanding cycling performance, maintaining 74.3% capacity retention after 800 cycles at 1C rate, as evidenced in Fig. 14e and f.

5.3 Electrolyte additive

In SIBs, the electrode–electrolyte interface (EEI) plays a crucial role in the stability of the electrode material and the diffusion of Na^+.[153,154] An unstable EEI implies an increase in harmful side reactions, structural damage after cycling, and dissolution of transition metal ions during cycling. Electrolyte additives are a simple, efficient and economical means of improving interfacial stability. During battery cycling, the additives are able to preferentially undergo oxidation reactions, based on which *in situ* modification of the electrode surface is achieved.[155,156] By rationally adjusting the type and concentration of electrolyte additives, it is possible to construct a CEI on the surface of PBAs that meets the specific needs, or replace the easily dissolved excess TM with a more stable TM, thus enhancing the electrochemical performance of the battery. Additionally, most practical applications of PBA-based SIBs employ low-cost carbonate-based electrolytes. However, these electrolytes suffer from poor thermal stability and high flammability, posing significant safety risks under extreme conditions such as thermal shock, overcharging, and short circuits.[157,158] To alleviate these issues, various non-flammable electrolyte additives have been designed. Non-flammable electrolyte additives function through dual mechanisms. They release phosphorus/halogen radicals to quench reactive oxygen species in combustion chain reactions. Simultaneously, thermal decomposition generates dense carbonized layers that isolate oxygen and suppress electrolyte vaporization. This combined action effectively mitigates the exothermic reactions driving battery thermal runaway.[159] Liu *et al.*[118] prepared a base electrolyte (G2) by dissolving a stoichiometric amount of $NaPF_6$ in diethylene glycol dimethyl ether (DEGDME) solvent with a fixed molar concentration of 1.0 M. Subsequently, a stable EEI was engineered through the incorporation of sodium difluorooxalato borate (NaDFOB) as a functional additive into the G2 electrolyte system. NaDFOB preferentially oxidized and strengthened the CEI layer at the cathode, preventing the oxidative decomposition of the electrolyte and dissolution of the TM, and preserving the stability of the material. The electrochemical performance of a self-assembled FeMnHCF||hard carbon (HC) 18650 cylindrical battery was evaluated in the G2+NaDFOB electrolyte. The results revealed that the initial coulombic efficiency (ICE) reached 85.4% with the NaDFOB additive, representing a significant improvement compared to the 70.9% ICE observed in pure G2 electrolyte. This enhancement demonstrates that NaDFOB effectively suppresses the oxidative decomposition of the solvent, thereby improving the initial charging efficiency of the battery system, as illustrated in Fig. 15a. By observing the HC anode surface through *ex situ* computed tomography (CT), no additional substances were observed during the charging process of the G2+NaDFOB electrolyte, indicating that NaDFOB plays a key role in stabilizing the EEI and suppressing continuous sodium precipitation (Fig. 15b). Meanwhile, due to the stable CEI layer and the inhibition of the dissolution of TM, the battery has good cycling stability (89.3% capacity retention after 100 cycles) (Fig. 15c). In addition, Kuang *et al.*[119] investigated the effect of the sulfur-containing additive sulfolane (SL) on the EEI. DFT calculations showed that SL has a higher highest occupied molecular orbital (HOMO, −7.79 eV) and a lower lowest unoccupied molecular orbital (LUMO, 0.42 eV) than the commonly used carbonate solvents, suggesting the preferential decomposition of SL to form the sulfur-containing EEI (Fig. 15d). TEM and XPS demonstrated that the addition of SL on the one hand enabled the PB to indicate the generation of a thin and homogeneous CEI after cycling, and on the other hand inhibited electrolyte decomposition and structural deformation of the PB (Fig. 15e and f).

Besides, Liang *et al.*[23] inhibited the dissolution of Mn during cycling by introducing sodium ferrocyanide ($Na_4Fe(CN)_6$) as an electrolyte additive. This was mainly attributed to the fact that $Fe(CN)_6^{4-}$ in $Na_4Fe(CN)_6$ can encapsulate on the surface of NaFeMnF particles, trapping migrated Mn *in situ*. Cycled EDS revealed that the addition of $Na_4Fe(CN)_6$ resulted in almost unchanged Mn content in the PB, whereas Mn in the blank electrolyte was significantly reduced. The cycling stability of the battery was significantly improved by the addition of $Na_4Fe(CN)_6$ (the capacity retention after 600 cycles was significantly increased from 54.6% to 95.6%). Yang *et al.*[160] developed a non-flammable sodium-ion battery electrolyte based on triethyl phosphate (TEP) by incorporating 5 wt% vinylene carbonate (VC) and regulating ion–dipole interactions. In Prussian blue||hard carbon pouch cells, this electrolyte demonstrated exceptional performance (96% capacity retention after 50 cycles at 50 mA g^{-1} with energy densities reaching 221.7 W h kg^{-1}). Additionally, it exhibited superior safety characteristics, including a high flash point (141 °C) and self-extinguishing behavior.

Overall, the interfacial modulation of PBAs plays a crucial role in their electrochemical and safety performance enhancement. A good EEI implies a stable interface, fewer side reactions, and almost no dissolution of TM, which implies an improvement in the cycling stability performance of the battery.

5.4 Co-regulation of the bulk and interface

The PBAs after bulk phase regulation have a good crystal structure and sufficient sodium storage sites, which enable Na^+ to migrate smoothly within the bulk phase. The optimized

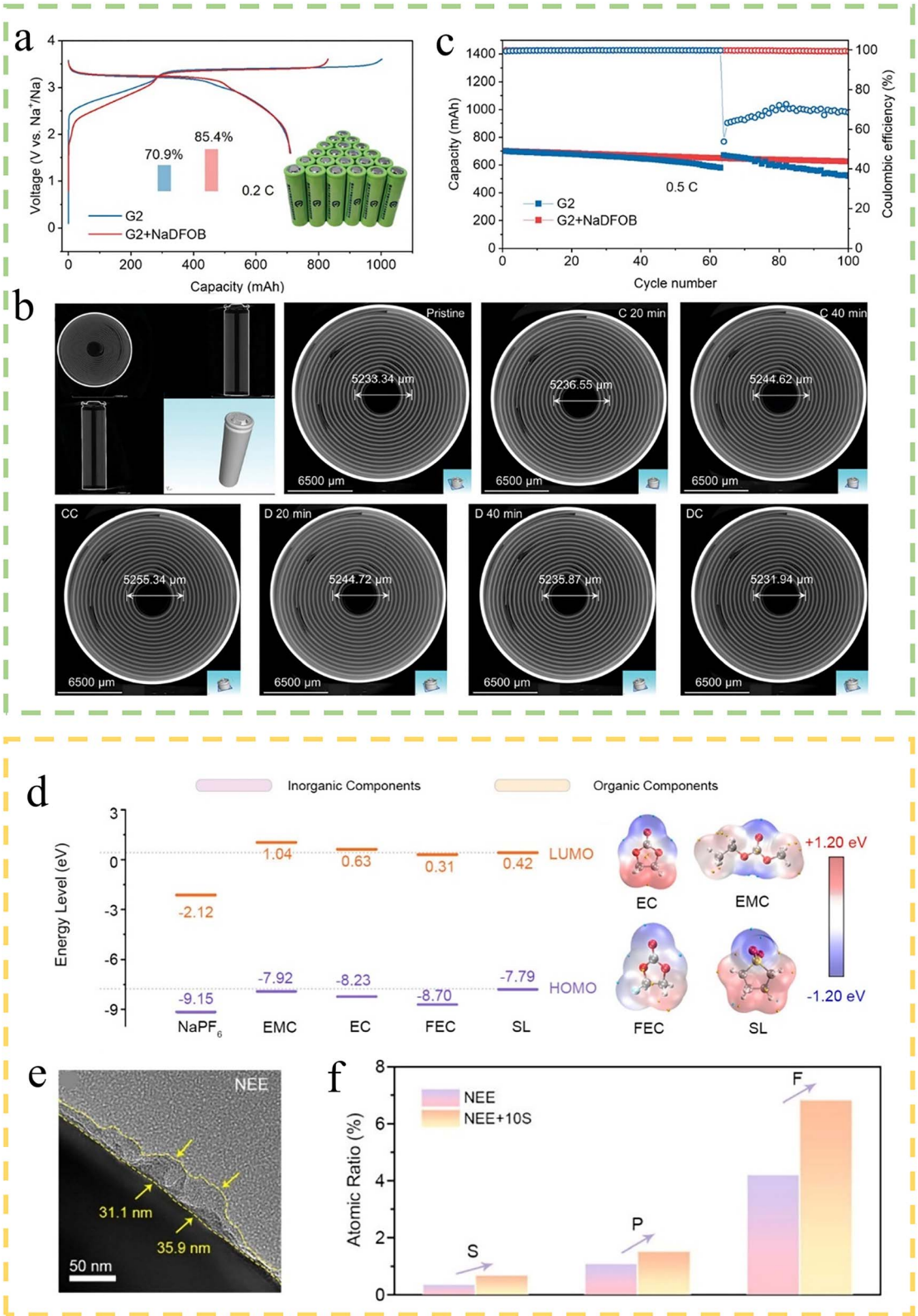

Fig. 15 (a) Charge and discharge profiles (inset: a digital photo of self-assembled FeMnHCF||HC 18650 cylindrical batteries). (b) Overall reconstruction of 18650 cylindrical batteries in the G2+NaDFOB electrolyte scanned by X-ray CT (accelerating voltage 150 kV) and cross-sections of jelly roll during the charge and discharge process (C: charge, CC: charge completed, D: discharge, DC: discharge completed). (c) Cycling stability with G2 and G2+NaDFOB electrolyte.[118] Copyright 2024, Wiley-VCH. (d) HOMO and LUMO energy levels of $NaPF_6$ salts, commonly used solvents/additives, and SL. (e) TEM images of cycled PB in a commercial ester-based electrolyte with added SL. (f) Atomic ratio of CEI on the PB surface after 100 cycles.[119] Copyright 2024, American Chemical Society.

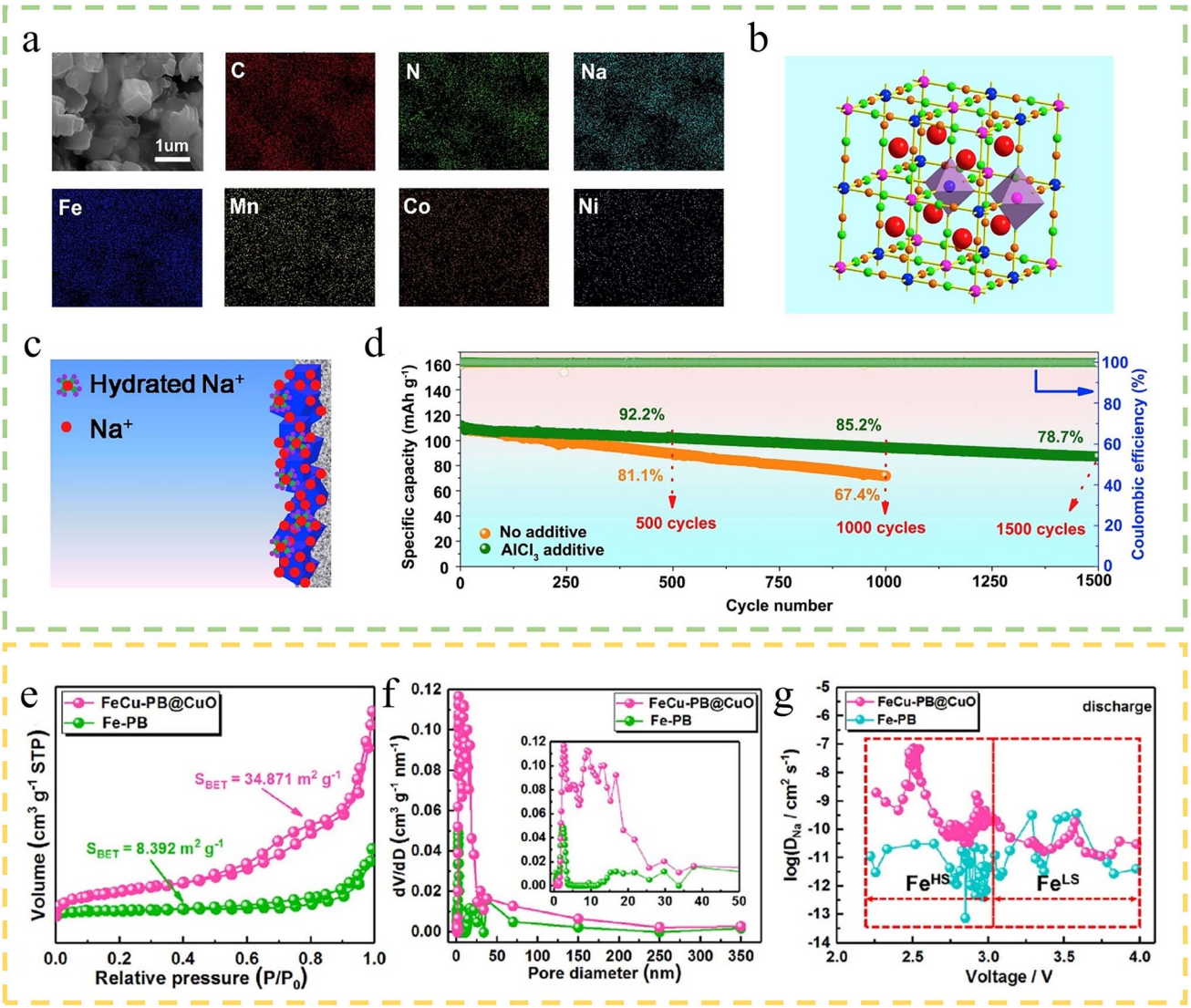

Fig. 16 (a) SEM and EDS of HQ-MnCoNi-PB. (b) Schematic crystal structure of the PB framework (the blue, orange, green, red and pink spheres respectively represent occupied sites of Fe^{LS}, C, N, Na and Fe^{HS} including partial doping of Mn^{HS}, Co^{HS} and Ni^{HS}, as well as the purple pyramid exhibiting octahedral configurations of Fe^{LS} and Fe^{HS}). (c) Schematic diagram of bare Na^+ and hydrated Na^+ migration in the HQ-MnCoNi-PB cathode. (d) Cycling performance of HQ-MnCoNi-PB with and without 1 wt% $AlCl_3$ electrolyte additive at 1C.[161] Copyright 2019, Elsevier. (e) N_2 adsorption–desorption isotherms of samples. (f) Pore size distribution curves of samples. The inset in panel (f) is the corresponding enlarged view. (g) Na^+ diffusion coefficients during the discharge process obtained from the GITT curves.[162] Copyright 2022, American Chemical Society.

interface environment, achieved through interface control engineering, facilitates rapid Na^+ transport across the EEI during both charge and discharge processes, while simultaneously minimizing interfacial side reactions. By regulating both the bulk phase and the interface of PBAs at the same time, the advantages of both can be brought into full play, and PBAs with high efficiency of Na^+ transport and storage can be obtained. Xie *et al.*[161] obtained HQ-MnCoNi-PB by using Mn, Co, Ni co-doping assisted by citric acid and the Lewis acid $AlCl_3$ as an electrolyte additive. EDS confirms the successful introduction of Mn, Co, and Ni (Fig. 16a). The doping of TMs regulated the lattice expansion, balanced the internal stresses, and stabilized the lattice framework (Fig. 16b). The Lewis acid $AlCl_3$ on the other hand, can capture the ligand water *in situ* and form a protective layer of $Al_2O_3 \cdot 3H_2O$ on the cathode (Fig. 16c). After synergistic modulation, the cycling stability of the composites was enhanced (81.8% retention after 500 cycles) (Fig. 16d). Chen *et al.*[162] prepared a Cu-modified Fe-PB composite (FeCu-PB@CuO) by modulating the crystal structure of Fe-PB through Cu doping and introducing a CuO coating for surface engineering. N_2 adsorption desorption isotherms indicate that the CuO coating increases the specific surface area (Fig. 16e). Calculation by the Barrett–Joyner–Halenda method shows that FeCu-PB@CuO has more mesopores, causing more Na^+ migration pathways (Fig. 16f). GITT proves the improvement of Na^+ diffusion coefficient (Fig. 16g). The initial capacity of FeCu-PB@CuO reached 123.5 mA h g^{-1} at 0.1 A g^{-1} and remained at 108.7 mA h g^{-1} after 200 cycles, and the capacity was

Table 2 The comparison of PBA sodium-ion half-cell systems in terms of testing voltage window, discharge capacity, cycling performance, and electrolyte[a]

Chemical formula	Voltage window [V *vs.* Na^+/Na]	Discharge capacity [mA h g^{-1} @ mA g^{-1}]	Capacity retention [retention, cycle @ mA g^{-1}]	Electrolyte	Ref.
$Na_{2-x}FeFe(CN)_6$	2.0–4.2	118 @ 100, ~128 @ 50	98.9%, 500 @ 100	1 M $NaClO_4$ in EC/PC (1 : 1), 3% FEC	49
$Na_{1.18}Fe[Fe(CN)_6]_{0.98}\square_{0.02}\cdot 2.41H_2O$	2.0–4.0	113.6 @ 30	85.5%, 1200 @ 300	1 M $NaClO_4$ in EC/PC (1 : 1), 5% FEC	120
$Na_{1.37}Fe[Fe(CN)_6]_{0.91}\cdot 1.65H_2O$	2.0–4.0	132.0 @ 100	~100%, 100 @ 100	1 M $NaClO_4$ in EC/PC (1 : 1), 5% FEC	121
$Na_{1.63}Mn_{0.25}Co_{0.22}Cu_{0.22}Ni_{0.01}Fe_{0.3}[Fe(CN)_6]_{0.943}$	2.0–4.0	122.5 @ 100, ~110 @ 1000	76.3%, 2000 @ 1000	1 M $NaClO_4$ in PC, 5% FEC	122
$Na_{1.6}Mn_{0.75}(\square Mn)_{0.25}[Fe(CN)_6]\cdot 1.57H_2O$	2.0–4.2	137.0 @ 25	72.3%, 2700 @ 500	1 M $NaPF_6$ in EC/PC (1 : 1), 2% FEC	123
$Na_{1.5}Cu_{0.038}Fe_{0.691}\square_{0.271}[Fe(CN)_6]$	2.0–4.2	132.4 @ 50, 115.8 @ 500	78.5%, 200 @ 500	1 M $NaClO_4$ in PC, 5% FEC	30
$Na_{1.53}Fe[Fe(CN)_6]_{0.86}\square_{0.14}\cdot 2.40H_2O$	2.0–4.2	131.0 @ 170	83.0%, 500 @ 170	1 M $NaClO_4$ in EC/DEC (1 : 1), 5% FEC	124
$Na_{1.98}Fe_{0.89}Zn_{0.11}[Fe(CN)_6]_{0.90}\square_{0.10}\cdot 1.60H_2O$	2.0–4.2	145.0 @ 20, 98.5 @ 1000	74.9%, 500 @ 1000	1 M $NaClO_4$ in EC/DEC/EMC (1 : 1 : 1), 2% FEC	129
$Na_{1.55}Zn_{0.36}Fe_{0.64}[Fe(CN)_6]$	2.0–4.2	95.4 @ 15	76.5%, 500 @ 150	1 M $NaClO_4$ in EC/DEC (1 : 1), 5% FEC	130
$Na_{1.96}Mn_{0.53}Ni_{0.47}[Fe(CN)_6]_{0.98}\cdot 1.81H_2O$	2.0–4.2	~100.0 @ 15	90.1%, 10 000 @ 150	1 M $NaClO_4$ in EC/DEC (1 : 1), 4% FEC	131
$K_{0.02}Na_{1.71}Fe_{0.66}Mn_{0.34}[Fe(CN)_6]_{0.97}\square_{0.03}\cdot 1.24H_2O$	2.0–4.2	139.1 @ 100	77.1%, 700 @ 100	0.8 M $NaClO_4$ in PC/EMC (50 : 45), 5% FEC	141
$Na_{0.28}K_{1.55}Fe[Fe(CN)_6]\cdot 1.53H_2O$	2.0–4.2	147.9 @ 15	83.5%, 300 @ 150	1 M $NaClO_4$ in EC/DEC (1 : 1), 5% FEC	26
$Na_{1.72}Mg_{0.04}K_{0.013}Mn_{0.64}Fe_{0.20}$ $Ni_{0.16}[Fe(CN)_6]_{0.95}\cdot 2.01H_2O$	2.0–4.0	115.8 @ 0.1C	93.9%, 500 @ 5C	1 M $NaPF_6$ in EMC/PC (1 : 1), 4% FEC	111
$Na_{1.96}Mn[Mn(CN)_6]_{0.99}\square_{0.01}\cdot 2H_2O$	1.4–4.0	209 @ 40	75%, 100 @ 400	N/A	144
$Mn[Fe(CN)_5NO]$	2.0–4.2	115.8 @ 100	82.1%, 400 @ 100	1 M $NaClO_4$ in EC/DMC/EMC (1 : 1 : 1), 5% FEC	145
$Na_{1.72}Ni[Fe(CN)_6]_{0.95}\square_{0.05}$	2.0–4.0	83.5 @ 15	94.0%, 1000 @ 75	1 M $NaPF_6$ in EC/DEC (1 : 1), 5% FEC	68
$Na_{1.13}Fe[Fe(CN)_6]_{0.79}\square_{0.21}\cdot 0.94H_2O$	2.0–4.2	109.7 @ 100	~80.0%, 200 @ 100	1 M $NaClO_4$ in EC/DMC/EMC (1 : 1 : 1), 2% FEC	112
$Na_{1.1}Fe[Fe(CN)_6]_{0.99}\square_{0.01}\cdot 2.62H_2O$–0.19ZnO	2.0–4.0	110.3 @ 45	91.5%, 200 @ 150	1 M $NaClO_4$ in EC/PC (1 : 1), 5% FEC	115
$Na_{1.96}Mn_{0.94}Ni_{0.06}[Fe(CN)_6]_{1.00}\cdot 1.37H_2O$	2.0–4.0	126.9 @ 0.1C	74.3%, 800 @ 1C	1 M $NaPF_6$ in EC/DEC (1 : 1)	117
$Na_{1.59}Mn_{0.17}Co_{0.18}Ni_{0.04}Fe_{0.61}[Fe(CN)_6]_{0.92}$	2.0–4.0	117.0 @ 17	81.1%, 500 @ 170	1 M $NaPF_6$ in EC/DEC (1 : 1), 8% FEC	161
$Na_{1.16}Fe_{0.98}Cu_{0.02}[Fe(CN)_6]_{0.94}\square_{0.06}\cdot 0.44H_2O$@0.04CuO	2.0–4.2	~122.0 @ 100	88.0%, 200 @ 100	1 M $NaClO_4$ in EC/DMC/EMC (1 : 1 : 1), 2% FEC	162
$Na_{1.65}Fe_{0.83}Mn_{0.1}Cu_{0.07}[Fe(CN)_6]_{0.94}\cdot 1.49H_2O$@PANI	2.0–4.0	116.9 @ 30	~90.0%, 500 @ 1000	1 M $NaClO_4$ in EC/DMC/EMC (1 : 1 : 1), 2% FEC	163

[a] EC: ethylene carbonate; PC: polypropylene carbonate; FEC: fluoroethylene carbonate; DEC: diethyl carbonate; DMC: dimethyl carbonate; EMC: ethyl methyl carbonate.

59.1 mA h g^{-1} after 1500 cycles at 2 A g^{-1}. Xu *et al.*[163] prepared FeMnCu Co-doped PB by a double iron source coprecipitation method, and coated it with the conductive polymer polyaniline (PANI) to form the core–shell structure FeMnCu@PANI. As the cathode material of SIBs, the electrochemical performance of the material is significantly improved. A two-pronged approach that combines the strengths of both regulations might be a promising approach to the challenges of PBA commercialization (Table 2).

6 Summary and outlook

Low-cost SIBs have come into prominence today with the focus on carbon neutrality and new energy development. As a promising cathode material among SIBs, PBAs show significant development potential due to their tunable structure, simple synthesis and low cost. This paper reviews the structure (crystal structure and phase structure), morphology and reaction mechanism of PBA materials. It then analyzed the current challenges to the commercialization of PBAs. These challenges include: crystal water and crystal defects, side reactions and thermal runaway, transition metal dissolution and structural collapse, as well as limitations in both energy density and power density. To address the above issues, the mainstream and low-cost modulation methods that can be practically applied to industrialization are reviewed, including bulk phase regulation, interface regulation and co-regulation of the bulk and interface. Bulk phase regulation is a critical strategy for enhancing the electrochemical performance of PBAs, addressing challenges such as low specific capacity, poor cycling stability, and low operating voltage through precise control of crystal structure, electronic properties, and ion transport kinetics. Through ion doping, it exerts precise control over the crystal structure of PBAs. Additionally, by regulating synthesis conditions, such as temperature and reaction rate, it can effectively reduce crystal defects and optimize crystallinity. These improvements enhance electronic conductivity and ion migration capability. Consequently, it substantially increases specific capacity, notably improves cycling stability, and significant boosts rate performance. Interface regulation also plays a pivotal role in enhancing battery performance by mitigating side reactions, optimizing CEI film formation, and inhibiting surface metal ion dissolution. Firstly, through precise interface engineering, undesirable side reactions can be effectively suppressed, leading to significant improvements in both cycling stability and safety. Secondly, interface modification facilitates the controlled formation of a stable and uniform CEI layer, which not only minimizes interfacial resistance but also promotes efficient ion transport, thereby enhancing rate capability and capacity retention. Furthermore, a well-designed interface effectively prevents the dissolution of metal ions from the cathode surface, reducing the loss of active materials and extending the overall lifespan of the battery. Co-regulation of the bulk and interface optimizes the crystal structure and interface environment of PBAs through the combination of two regulation methods, achieving better comprehensive performance. This regulatory approach is receiving increasing attention and is expected to play an important role in the industrialization process of PBAs.

Although the current research on PBAs has made some progress, there are still some challenges for their large-scale industrialization. Future prospects for the development of PBAs in energy storage are as follows:

6.1 Exploration of the intrinsic mechanism of PBAs

In the field of SIBs, PBAs have many unclear mechanisms, such as the details of sodium storage mechanisms, the specific coordination environment of Na^+ in the lattice and its impact on sodium storage performance. It is unclear whether the mechanism of high-temperature calcination activation of low-spin Fe under nitrogen is universal in the reaction process of low-spin Fe, and whether its redox activity, spin state, and other changes in long-term cycling are clear. At the bulk phase level, further exploration is needed for the specific mechanisms and dynamic changes of different forms of crystal water, as well as the formation mechanisms, distribution patterns, and regulation methods of vacancies. As for the electrode interface, the mechanism of side reactions, as well as the formation process and growth mechanism of CEI films, require further study. At the same time, the specific mechanism of capacitance attenuation under high current density and the mechanism of performance optimization strategies such as surface coatings and composite materials urgently need further research.

6.2 Exploration of large-scale and low-cost synthesis and coating processes

The low cost of raw materials and simple preparation are the key reasons why PBAs stand out among mainstream cathode materials. In future development, scaling up production while ensuring low cost is crucial. Developing green synthesis technology, simplifying the synthesis process (*e.g.*, washing-free mechanochemical method) and exploring the use of renewable resources (*e.g.*, waste recycling) as a source of raw materials are all elements that need to be explored, as shown in Fig. 17. At the same time, innovative coating processes such as dry coating should be actively explored, as their solvent-free processing characteristics can effectively avoid the pollution risks of traditional wet processes, while reducing equipment complexity and improving manufacturing efficiency.

6.3 Responding to extreme conditions in practical applications

In practical battery applications, various extreme operational conditions must be considered. Low temperature will increase the viscosity of the electrolyte inside the battery, reducing the rate of ionic conduction; high temperature will accelerate the rate of chemical reaction inside the battery, so that the battery generates a lot of heat; undulating steep slopes require the battery to have a strong power output stability and durability. Stable operation under such extreme conditions will be the distinguishing feature of PBAs compared to other materials (Fig. 17). In this regard, it is necessary to pay attention to the thermal stability of the material and explore suitable

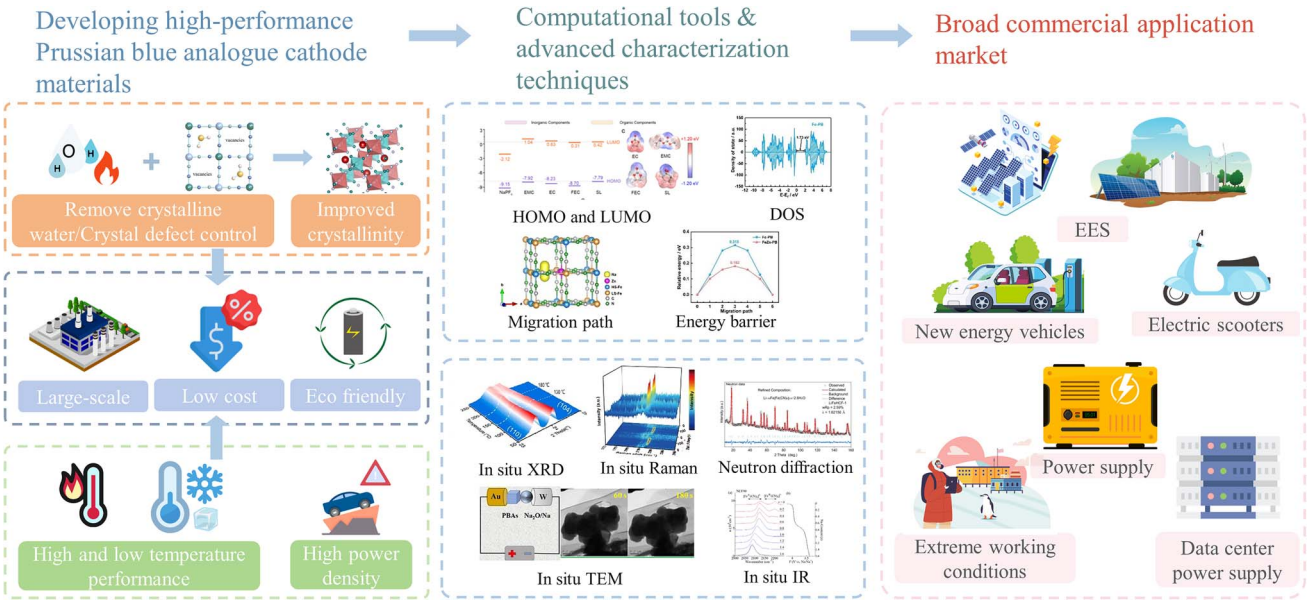

Fig. 17 Future prospects for the commercialization process of PBAs.

electrolytes to improve the interfacial stability. Improvements in rate performance can also be achieved by optimizing particle size, morphology and electrode configuration (*e.g.*, thin film electrodes).

6.4 Combining theoretical calculations with advanced characterization techniques

In the process of exploring the intrinsic mechanism of PBAs and designing suitable optimization methods, theory and practice can be combined. At the same time, advanced characterization techniques can be used to realize the detailed analysis of PBAs. As shown in Fig. 17, DFT calculations can be used to predict the migration paths and active sites of Na^+ in PBAs, guiding the optimization of material structural design and establishing more accurate theoretical models by combining with experimental data. *In situ* XRD and *in situ* TEM can monitor changes in the material's crystal structure during charging and discharging in real time, revealing the reaction mechanism. And neutron scattering can be used to further investigate the specific embedding locations and channels of Na^+. In the future, it can also be combined with multi-scale characterization techniques to systematically study the performance of the materials and provide theoretical and experimental basis.

6.5 Combination of laboratory and production line

It is crucial to match the performance indicators of materials with industrial requirements. In the absence of practical application, the true value of materials science research through studying materials cannot be realized. Researchers should not only be able to apply advanced equipment to analyze materials, but also focus on the production line information, such as the median particle size of the material, porosity, compaction density and vibration density, surface density and so on. By integrating both laboratory data and production line information, the research results of materials science can be effectively transformed into marketable products.

6.6 Artificial intelligence-driven PBA material engineering

The development of PBAs could be revolutionized through the integration of artificial intelligence (AI) and high-throughput computational screening. Machine learning models trained on quantum chemistry datasets can predict formation energies, Na^+ migration barriers, and interface stability with unprecedented efficiency. This predictive capability accelerates the discovery of novel doping elements and electrolyte additives. Additionally, generative adversarial networks (GANs) enable inverse design of PBAs with tailored vacancy distributions and controlled water content. Combined with AI driven autonomous laboratory design experiments to optimize synthesis parameters, non-traditional preparation pathways beyond traditional chemical intuition may be discovered.

In the past, solely regulating the bulk phase or interface of PBAs often addressed only one issue, thereby limiting their broader commercial applications. Recent studies have integrated bulk phase and interface regulation, showing enhanced electrochemical performance. Future research is expected to demonstrate that the joint regulation of the bulk phase and interface will likely play a significant synergistic role. This review provides valuable insights and strategic guidelines for the rational design of high-performance PBA cathodes toward practical implementation. With continued research efforts and technological advancements, PBAs are anticipated to realize their full potential as promising candidates for next-generation energy storage and conversion systems.

Data availability

Data sharing is not applicable to this article as no new data were created or analyzed in this study.

Author contributions

Boao Zhou: writing – original draft, methodology, formal analysis. Yun Gao: writing – review & editing. Xihao Lin: data curation. Bin Yang: review & editing, supervision. Ning Kang: writing – review & editing, supervision. Yun Qiao: writing – review & editing, supervision. Hang Zhang: writing – review & editing, supervision, data curation. Li Li: writing – review & editing, supervision, project administration, funding acquisition. Shulei Chou: writing – review & editing, supervision, project administration, funding acquisition.

Conflicts of interest

The authors declare no conflict of interest.

Acknowledgements

This work was supported by the National Natural Science Foundation of China (No. 52250710680, No. 52402213, No. 52171217), Zhejiang Provincial Natural Science Foundation of China (No. ZCLY24E0201, LQN25E020015, LQN25B010007), Basic Research Project of WenZhou City (2024G0197, 2024G0195, G20240014), China Postdoctoral Science Foundation (Grant Numbers: 2023M740011, GZC20230009), and High-end Foreign Experts Recruitment Plan of China (S20240005).

References

1 B. Dunn, H. Kamath and J.-M. Tarascon, Electrical Energy Storage for the Grid: A Battery of Choices, *Science*, 2011, **334**, 928–935.
2 F. Duffner, N. Kronemeyer, J. Tübke, J. Leker, M. Winter and R. Schmuch, Post-lithium-ion battery cell production and its compatibility with lithium-ion cell production infrastructure, *Nat. Energy*, 2021, **6**, 123–134.
3 C. Jiang, Y. Wang, Y. Xin, X. Ding, S. Liu, Y. Pang, B. Chen, Y. Wang, L. Liu, F. Wu and H. Gao, Toward high stability of O3-type NaNi1/3Fe1/3Mn1/3O2 cathode material with zirconium substitution for advanced sodium-ion batteries, *Carbon Neutralization*, 2024, **3**, 233–244.
4 Y. Gao, H. Zhang, X.-H. Liu, Z. Yang, X.-X. He, L. Li, Y. Qiao and S.-L. Chou, Low-Cost Polyanion-Type Sulfate Cathode for Sodium-Ion Battery, *Adv. Energy Mater.*, 2021, **11**, 2101751.
5 P.-F. Wang, H.-R. Yao, X.-Y. Liu, J.-N. Zhang, L. Gu, X.-Q. Yu, Y.-X. Yin and Y.-G. Guo, Ti-Substituted $NaNi_{0.5}Mn_{0.5}$-TiO_2 Cathodes with Reversible O3−P3 Phase Transition for High-Performance Sodium-Ion Batteries, *Adv. Mater.*, 2017, **29**, 1700210.
6 N. Yabuuchi, K. Kubota, M. Dahbi and S. Komaba, Research Development on Sodium-Ion Batteries, *Chem. Rev.*, 2014, **114**, 11636–11682.
7 H. Zhang, Y. Gao, X. Liu, L. Zhou, J. Li, Y. Xiao, J. Peng, J. Wang and S.-L. Chou, Long-Cycle-Life Cathode Materials for Sodium-Ion Batteries toward Large-Scale Energy Storage Systems, *Adv. Energy Mater.*, 2023, **13**, 2300149.
8 A. Rudola, R. Sayers, C. J. Wright and J. Barker, Opportunities for moderate-range electric vehicles using sustainable sodium-ion batteries, *Nat. Energy*, 2023, **8**, 215–218.
9 Z. Liu, C. Peng, J. Wu, T. Yang, J. Zeng, F. Li, A. Kucernak, D. Xue, Q. Liu and M. Zhu, Regulating electron distribution of P2-type layered oxide cathodes for practical sodium-ion batteries, *Mater. Today*, 2023, **68**, 22–33.
10 W. Zuo, A. Innocenti, M. Zarrabeitia, D. Bresser, Y. Yang and S. Passerini, Layered oxide cathodes for sodium-ion batteries: storage mechanism, electrochemistry, and techno-economics, *Acc. Chem. Res.*, 2023, **56**, 284–296.
11 J.-Y. Hwang, S.-T. Myung and Y.-K. Sun, Sodium-ion batteries: present and future, *Chem. Soc. Rev.*, 2017, **46**, 3529–3614.
12 T. Jin, H. Li, K. Zhu, P.-F. Wang, P. Liu and L. Jiao, Polyanion-type cathode materials for sodium-ion batteries, *Chem. Soc. Rev.*, 2020, **49**, 2342–2377.
13 Y.-F. Liu, K. Han, D.-N. Peng, L.-Y. Kong, Y. Su, H.-W. Li, H.-Y. Hu, J.-Y. Li, H.-R. Wang, Z.-Q. Fu, Q. Ma, Y.-F. Zhu, R.-R. Tang, S.-L. Chou, Y. Xiao and X.-W. Wu, Layered oxide cathodes for sodium-ion batteries: From air stability, interface chemistry to phase transition, *InfoMat*, 2023, **5**, e12422.
14 Y. Sun, S. Guo and H. Zhou, Adverse effects of interlayer-gliding in layered transition-metal oxides on electrochemical sodium-ion storage, *Energy Environ. Sci.*, 2019, **12**, 825–840.
15 Y.-K. Sun, Direction for Commercialization of O3-Type Layered Cathodes for Sodium-Ion Batteries, *ACS Energy Lett.*, 2020, **5**, 1278–1280.
16 T. Song, C. Wang and C.-S. Lee, Structural degradation mechanisms and modulation technologies of layered oxide cathodes for sodium-ion batteries, *Carbon Neutralization*, 2022, **1**, 68–92.
17 Q. Ni, Y. Bai, F. Wu and C. Wu, Polyanion-Type Electrode Materials for Sodium-Ion Batteries, *Adv. Sci.*, 2017, **4**, 1600275.
18 X.-H. Liu, W.-H. Lai, J. Peng, Y. Gao, H. Zhang, Z. Yang, X.-X. He, Z. Hu, L. Li, Y. Qiao, M.-H. Wu and H.-K. Liu, A NASICON-typed $Na_4Mn_{0.5}Fe_{0.5}Al(PO_4)_3$ cathode for low-cost and high-energy sodium-ion batteries, *Carbon Neutralization*, 2022, **1**, 49–58.
19 A. Simonov, T. De Baerdemaeker, H. L. B. Boström, M. L. Ríos Gómez, H. J. Gray, D. Chernyshov, A. Bosak, H.-B. Bürgi and A. L. Goodwin, Hidden diversity of vacancy networks in Prussian blue analogues, *Nature*, 2020, **578**, 256–260.
20 Y. Zeng, J. Xu, Y. Wang, S. Li, D. Luan and X. W. Lou, Formation of CuMn Prussian Blue Analog Double-Shelled Nanoboxes Toward Long-Life Zn-ion Batteries, *Angew. Chem., Int. Ed.*, 2022, **61**, e202212031.
21 Y. Gao, X. Zhang, H. Zhang, J. Peng, W. Hua, Y. Xiao, X.-H. Liu, L. Li, Y. Qiao, J.-Z. Wang, C. Zhang and S. Chou, Zero-Waste Polyanion and Prussian Blue

Composites toward Practical Sodium-Ion Batteries, *Adv. Mater.*, 2025, **37**, 2409782.

22 Y. Luo, J. Shen, Y. Yao, J. Dai, F. Ling, L. Li, Y. Jiang, X. Wu, X. Rui and Y. Yu, Inhibiting the Jahn–Teller Effect of Manganese Hexacyanoferrate *via* Ni and Cu Codoping for Advanced Sodium-Ion Batteries, *Adv. Mater.*, 2024, **36**, 2405458.

23 Z. Liang, F. Tian, G. Yang and C. Wang, Enabling long-cycling aqueous sodium-ion batteries *via* Mn dissolution inhibition using sodium ferrocyanide electrolyte additive, *Nat. Commun.*, 2023, **14**, 3591.

24 T. Liu, H. Wu, X. Du, J. Wang, Z. Chen, H. Wang, J. Sun, J. Zhang, J. Niu, L. Yao, J. Zhao and G. Cui, Water-Locked Eutectic Electrolyte Enables Long-Cycling Aqueous Sodium-Ion Batteries, *ACS Appl. Mater. Interfaces*, 2022, **14**, 33041–33051.

25 B. Yuan, S. Qiao, L. Yuan, B. Chen and S. Chong, Zero-Strain Sodium Nickel Ferrocyanide as Cathode Material for Sodium-Ion Batteries with Ultra-Long Lifespan, *Small*, 2024, **21**, 2407570.

26 L. Li, J. Shen, H. Yang, Z. Li, Z. Chen, Y. Yao, W. Li, X. Wu, X. Rui and Y. Yu, Selection Rules of Transition Metal Dopants for Prussian Blue Analogs Enabling Highly Reversible Sodium Storage, *Adv. Energy Mater.*, 2024, **14**, 2401729.

27 H. Ma, M. Jiang, Z. Hou, T. Li, X. Zhang, Y. Gao, J. Peng, Y. Li and J.-G. Wang, Medium-mediated high-crystalline Prussian blue toward exceptionally boosted sodium energy storage, *Energy Storage Mater.*, 2024, **70**, 103411.

28 S. He, J. Zhao, X. Rong, C. Xu, Q. Zhang, X. Shen, X. Qi, Y. Li, X. Li, Y. Niu, X. Li, S. Han, L. Gu, H. Liu and Y.-S. Hu, Solvent-free mechanochemical synthesis of Na-rich Prussian white cathodes for high-performance Na-ion batteries, *Chem. Eng. J.*, 2022, **428**, 131083.

29 F. Peng, L. Yu, P. Gao, X.-Z. Liao, J. Wen, Y.-s. He, G. Tan, Y. Ren and Z.-F. Ma, Highly crystalline sodium manganese ferrocyanide microcubes for advanced sodium ion battery cathodes, *J. Mater. Chem. A*, 2019, **7**, 22248–22256.

30 J. Liu, J. Liu, M. Tang, J. Fu, X. Kuang and J. Ma, Boosting Sodium Storage in Prussian Blue Analogs Through Iron Vacancies and Copper Doping, *Adv. Funct. Mater.*, 2024, **34**, 2314167.

31 N. Yabuuchi, M. Kajiyama, J. Iwatate, H. Nishikawa, S. Hitomi, R. Okuyama, R. Usui, Y. Yamada and S. Komaba, P2-type $Na_x[Fe_{1/2}Mn_{1/2}]O_2$ made from earth-abundant elements for rechargeable Na batteries, *Nat. Mater.*, 2012, **11**, 512–517.

32 F. Ding, C. Zhao, D. Xiao, X. Rong, H. Wang, Y. Li, Y. Yang, Y. Lu and Y.-S. Hu, Using High-Entropy Configuration Strategy to Design Na-Ion Layered Oxide Cathodes with Superior Electrochemical Performance and Thermal Stability, *J. Am. Chem. Soc.*, 2022, **144**, 8286–8295.

33 C. Chen, W. Huang, Y. Li, M. Zhang, K. Nie, J. Wang, W. Zhao, R. Qi, C. Zuo, Z. Li, H. Yi and F. Pan, P2/O3 biphasic Fe/Mn-based layered oxide cathode with ultrahigh capacity and great cyclability for sodium ion batteries, *Nano Energy*, 2021, **90**, 106504.

34 J. Jin, Y. Liu, X. Zhao, H. Liu, S. Deng, Q. Shen, Y. Hou, H. Qi, X. Xing, L. Jiao and J. Chen, Annealing in Argon Universally Upgrades the Na-Storage Performance of Mn-Based Layered Oxide Cathodes by Creating Bulk Oxygen Vacancies, *Angew. Chem., Int. Ed.*, 2023, **62**, e202219230.

35 W. Lu, H. zhao, R. A. Soomro, N. Sun and B. Xu, Lattice sulfuration enhanced sodium storage performance of $Na_{0.9}Li_{0.1}Zn_{0.05}Ni_{0.25}Mn_{0.6}O_2$ cathode, *Chem. Eng. J.*, 2024, **501**, 157663.

36 N. Li, W. Yin, B. Wang, F. Wang, X. Xiao, J. Zhao and E. Zhao, Lowering Sodium-Storage Lattice Strains of Layered Oxide Cathodes by Pushing Charge Transfer on Anions, *Energy Environ. Mater.*, 2024, **7**, e12671.

37 N. Zhang, X. Dong, Q. Yan, J. Wang, F. Jin, J. Liu, D. Wang, H. Liu, B. Wang and S. Dou, High-entropy doping NASICONCathode breaks the kinetic barriers and suppresses voltage hysteresis for sodium ion batteries, *Energy Storage Mater.*, 2024, **72**, 103734.

38 Z.-Y. Gu, J.-Z. Guo, J.-M. Cao, X.-T. Wang, X.-X. Zhao, X.-Y. Zheng, W.-H. Li, Z.-H. Sun, H.-J. Liang and X.-L. Wu, An Advanced High-Entropy Fluorophosphate Cathode for Sodium-Ion Batteries with Increased Working Voltage and Energy Density, *Adv. Mater.*, 2022, **34**, 2110108.

39 X. Li, Y. Zhang, B. Zhang, K. Qin, H. Liu and Z.-F. Ma, Mn-doped $Na_4Fe_3(PO_4)_2(P_2O_7)$ facilitating Na^+ migration at low temperature as a high performance cathode material of sodium ion batteries, *J. Power Sources*, 2022, **521**, 230922.

40 N. Jiang, C. Yang, Y. Wang, X. Wang, J. Liu and Y. Liu, A Mn-based ternary NASICON-type $Na_{3.5}MnTi_{0.5}Cr_{0.5}(PO_4)_3$/C cathode for high-performance sodium-ion batteries, *Energy Storage Mater.*, 2023, **63**, 102978.

41 A. Plewa, A. Kulka, E. Hanc, W. Zając, J. Sun, L. Lu and J. Molenda, Facile aqueous synthesis of high performance $Na_2FeM(SO_4)_3$ (M = Fe, Mn, Ni) alluaudites for low cost Na-ion batteries, *J. Mater. Chem. A*, 2020, **8**, 2728–2740.

42 Q. Wei, X. Chang, J. Wang, T. Huang, X. Huang, J. Yu, H. Zheng, J.-h. Chen and D.-L. Peng, An Ultrahigh-Power Mesocarbon Microbeads|Na^+-Diglyme|$Na_3V_2(PO_4)_3$ Sodium-Ion Battery, *Adv. Mater.*, 2022, **34**, 2108304.

43 A. Kraft, What a chemistry student should know about the history of Prussian blue, *ChemTexts*, 2018, **4**, 16.

44 S. Qiu, Y. Xu, X. Wu and X. Ji, Prussian Blue Analogues as Electrodes for Aqueous Monovalent Ion Batteries, *Electrochem. Energy Rev.*, 2022, **5**, 242–262.

45 Y. Tang, W. Li, P. Feng, M. Zhou, K. Wang, Y. Wang, K. Zaghib and K. Jiang, High-Performance Manganese Hexacyanoferrate with Cubic Structure as Superior Cathode Material for Sodium-Ion Batteries, *Adv. Funct. Mater.*, 2020, **30**, 1908754.

46 W. Shu, C. Han and X. Wang, Prussian Blue Analogues Cathodes for Nonaqueous Potassium-Ion Batteries: Past, Present, and Future, *Adv. Funct. Mater.*, 2024, **34**, 2309636.

47 D. Kim, T. Hwang, J.-M. Lim, M.-S. Park, M. Cho and K. Cho, Hexacyanometallates for sodium-ion batteries: insights into higher redox potentials using d electronic

spin configurations, *Phys. Chem. Chem. Phys.*, 2017, **19**, 10443–10452.
48 A. Kumar, S. M. Yusuf and L. Keller, Structural and magnetic properties of $Fe[Fe(CN)_6]\cdot 4H_2O$, *Phys. Rev. B: Condens. Matter Mater. Phys.*, 2005, **71**, 054414.
49 W. Wang, Y. Gang, J. Peng, Z. Hu, Z. Yan, W. Lai, Y. Zhu, D. Appadoo, M. Ye, Y. Cao, Q.-F. Gu, H.-K. Liu, S.-X. Dou and S.-L. Chou, Effect of Eliminating Water in Prussian Blue Cathode for Sodium-Ion Batteries, *Adv. Funct. Mater.*, 2022, **32**, 2111727.
50 Z. Wang, Y. Huang, D. Chu, C. Li, Y. Zhang, F. Wu, L. Li, M. Xie, J. Huang and R. Chen, Continuous Conductive Networks Built by Prussian Blue Cubes and Mesoporous Carbon Lead to Enhanced Sodium-Ion Storage Performances, *ACS Appl. Mater. Interfaces*, 2021, **13**, 38202–38212.
51 J. Guo, F. Feng, S. Zhao, Z. Shi, R. Wang, M. Yang, F. Chen, S. Chen, Z.-F. Ma and T. Liu, High FeLS(C) electrochemical activity of an iron hexacyanoferrate cathode boosts superior sodium ion storage, *Carbon Energy*, 2023, **5**, e314.
52 A. Zhou, W. Cheng, W. Wang, Q. Zhao, J. Xie, W. Zhang, H. Gao, L. Xue and J. Li, Hexacyanoferrate-Type Prussian Blue Analogs: Principles and Advances Toward High-Performance Sodium and Potassium Ion Batteries, *Adv. Energy Mater.*, 2021, **11**, 2000943.
53 X. Wu, M. Sun, S. Guo, J. Qian, Y. Liu, Y. Cao, X. Ai and H. Yang, Vacancy-Free Prussian Blue Nanocrystals with High Capacity and Superior Cyclability for Aqueous Sodium-Ion Batteries, *ChemNanoMat*, 2015, **1**, 188–193.
54 Z. Zhou, Y. Qian, X. Chen, J. Chen, X. Zhou, W. Kuang, X. Shi, X. Wu, L. Li, J. Wang and S. Chou, Challenges and Strategies toward Manganese Hexacyanoferrate for High-Performance Sodium-Ion Batteries, *Adv. Funct. Mater.*, 2024, **34**, 2404938.
55 F. Gebert, D. L. Cortie, J. C. Bouwer, W. Wang, Z. Yan, S. X. Dou and S. L. Chou, Epitaxial Nickel Ferrocyanide Stabilizes Jahn–Teller Distortions of Manganese Ferrocyanide for Sodium-Ion Batteries, *Angew. Chem., Int. Ed.*, 2021, **60**, 18519–18526.
56 X.-H. Liu, J. Peng, W.-H. Lai, Y. Gao, H. Zhang, L. Li, Y. Qiao and S.-L. Chou, Advanced Characterization Techniques Paving the Way for Commercialization of Low-Cost Prussian Blue Analog Cathodes, *Adv. Funct. Mater.*, 2022, **32**, 2108616.
57 T. Shao, C. Li, C. Liu, W. Deng, W. Wang, M. Xue and R. Li, Electrolyte regulation enhances the stability of Prussian blue analogues in aqueous Na-ion storage, *J. Mater. Chem. A*, 2019, **7**, 1749–1755.
58 L. Shen, Y. Jiang, Y. Liu, J. Ma, T. Sun and N. Zhu, High-stability monoclinic nickel hexacyanoferrate cathode materials for ultrafast aqueous sodium ion battery, *Chem. Eng. J.*, 2020, **388**, 124228.
59 W. Ren, X. Chen and C. Zhao, Ultrafast Aqueous Potassium-Ion Batteries Cathode for Stable Intermittent Grid-Scale Energy Storage, *Adv. Energy Mater.*, 2018, **8**, 1801413.
60 G. Ni, B. Han, Q. Li, Z. Ji, B. Huang and C. Zhou, Instability of Zinc Hexacyanoferrate Electrode in an Aqueous Environment: Redox-Induced Phase Transition, Compound Dissolution, and Inhibition, *ChemElectroChem*, 2016, **3**, 798–804.
61 Y. Tan, Z. Chen, Z. Tao, A. Wang, S. Lai, S. Ho and Y. Yang, Anion electrostatic insertion boosts efficient zinc ferrocyanide cathode for aqueous dual-ion battery, *Energy Storage Mater.*, 2024, **67**, 103274.
62 S. Cao, Y. Li, Y. Tang, Y. Sun, W. Li, X. Guo, F. Yang, G. Zhang, H. Zhou, Z. Liu, Q. Li, M. Shakouri and H. Pang, Space-Confined Metal Ion Strategy for Carbon Materials Derived from Cobalt Benzimidazole Frameworks with High Desalination Performance in Simulated Seawater, *Adv. Mater.*, 2023, **35**, 2301011.
63 X. Chen, C. Hua, K. Zhang, H. Sun, S. Hu and Z. Jian, Control of Gradient Concentration Prussian White Cathodes for High-Performance Potassium-Ion Batteries, *ACS Appl. Mater. Interfaces*, 2023, **15**, 47125–47134.
64 K. Du, Y. Liu, Y. Zhao, H. Li, H. Liu, C. Sun, M. Han, T. Ma and Y. Hu, High-Entropy Prussian Blue Analogues Enable Lattice Respiration for Ultrastable Aqueous Aluminum-Ion Batteries, *Adv. Mater.*, 2024, **36**, 2404172.
65 Y. Xu, M. Ou, Y. Liu, J. Xu, X. Sun, C. Fang, Q. Li, J. Han and Y. Huang, Crystallization-induced ultrafast Na-ion diffusion in nickel hexacyanoferrate for high-performance sodium-ion batteries, *Nano Energy*, 2020, **67**, 104250.
66 S. Wu, X. Shen, H. Zhou, G. Zhu, R. Wang, Z. Ji, K. Chen and C. Chen, Morphological synthesis of Prussian blue analogue $Zn_3[Fe(CN)_6]_2\cdot xH_2O$ micro-/nanocrystals and their excellent adsorption performance toward methylene blue, *J. Colloid Interface Sci.*, 2016, **464**, 191–197.
67 J. Han, Y. Hu, Q. Han, X. Liu and C. Wang, Synthesis of high-specific-capacity Prussian blue analogues for sodium-ion batteries boosted by grooved structure, *J. Alloys Compd.*, 2023, **950**, 169928.
68 Y. Zhao, J. Peng, K. Chen, L. Luo, H. Chen, H. Zhang, S. Chou, X. Feng, W. Chen, R. Cao, X. Ai, Y. Fang and Y. Cao, Boosting the sodium storage performance of Prussian blue analogues *via* effective etching, *Sci. China: Chem.*, 2023, **66**, 3154–3160.
69 R. Guo, B. Xi, C. Guo, H. Zhang, L. Chen, W. Liu, N. Lv and J. Xu, Facet-Dependent Catalytic Activity of MnFe Prussian Blue Analogues in Peroxymonosulfate-Activated System for Efficient Degradation of Acetamiprid, *ACS ES&T Water*, 2023, **3**, 598–607.
70 P. Zhu, Y. Wang, J. Li and Y. Jin, Continuous Production of High-Capacity Iron-Based Prussian Blue Sodium-Ion Cathode Materials Using a Rotor-Stator Spinning Disk Reactor, *ACS Appl. Energy Mater.*, 2023, **6**, 6141–6150.
71 B. Huang, Y. Shao, Y. Liu, Z. Lu, X. Lu and S. Liao, Improving Potassium-Ion Batteries by Optimizing the Composition of Prussian Blue Cathode, *ACS Appl. Energy Mater.*, 2019, **2**, 6528–6535.
72 Z. Qin, B. Chen, Y. Mao, C. Shi, Y. Li, X. Huang, F. Yang and N. Gu, Achieving Ultrasmall Prussian Blue Nanoparticles as High-Performance Biomedical Agents with Multifunctions, *ACS Appl. Mater. Interfaces*, 2020, **12**, 57382–57390.

73 Q. Ying, S. Ni, H. Zhang, F. Yu and Y. Yang, Boosting Synergy of Polymetal Phosphides by Core-Shell Design of Prussian Blue Analogue Precursors as Electrocatalysts for Water Splitting, *ChemCatChem*, 2022, **14**, e202200330.
74 B. Zhao, Y. Wang, Z. Wang, Y. Hu, J. Zhang and X. Bai, Rational design of Core-Shell heterostructured CoFe@NiFe Prussian blue analogues for efficient capacitive deionization, *Chem. Eng. J.*, 2024, **487**, 150437.
75 E. Gabriel, C. Ma, K. Graff, A. Conrado, D. Hou and H. Xiong, Heterostructure engineering in electrode materials for sodium-ion batteries: Recent progress and perspectives, *eScience*, 2023, **3**, 100139.
76 X. Hu, W. Jian, N. Hong, X. Zhong, M. Yang, S. Tao, J. Huang, H. Wang, J. Gao, W. Deng, G. Zou, H. Hou, D. S. Silvester, C. E. Banks and X. Ji, Confined Element Distribution with Structure-Driven Energy Coupling for Enhanced Prussian Blue Analogue Cathode, *Angew. Chem., Int. Ed.*, 2024, **63**, e202410420.
77 W. Lu, X. Guo, Y. Luo, Q. Li, R. Zhu and H. Pang, Core-shell materials for advanced batteries, *Chem. Eng. J.*, 2019, **355**, 208–237.
78 S. Wang, W. Huo, H. Feng, Z. Xie, J. K. Shang, E. V. Formo, P. H. C. Camargo, F. Fang and J. Jiang, Enhancing Oxygen Evolution Reaction Performance in Prussian Blue Analogues: Triple-Play of Metal Exsolution, Hollow Interiors, and Anionic Regulation, *Adv. Mater.*, 2023, **35**, 2304494.
79 X. Jia, X. Cai, Y. Chen, S. Wang, H. Xu, K. Zhang, M. Ma, H. Wu, J. Shi and H. Chen, Perfluoropentane-encapsulated hollow mesoporous Prussian blue nanocubes for activated ultrasound imaging and photothermal therapy of cancer, *ACS Appl. Mater. Interfaces*, 2015, **7**, 4579–4588.
80 T. Huang, Y. Niu, Q. Yang, W. Yang and M. Xu, Self-Template Synthesis of Prussian Blue Analogue Hollow Polyhedrons as Superior Sodium Storage Cathodes, *ACS Appl. Mater. Interfaces*, 2021, **13**, 37187–37193.
81 W. Zhang, H. Song, Y. Cheng, C. Liu, C. Wang, M. A. N. Khan, H. Zhang, J. Liu, C. Yu, L. Wang and J. Li, Core–Shell Prussian Blue Analogs with Compositional Heterogeneity and Open Cages for Oxygen Evolution Reaction, *Adv. Sci.*, 2019, **6**, 1801901.
82 L. Yu, H. Hu, H. B. Wu and X. W. Lou, Complex Hollow Nanostructures: Synthesis and Energy-Related Applications, *Adv. Mater.*, 2017, **29**, 1604563.
83 L. Zhou, Z. Zhuang, H. Zhao, M. Lin, D. Zhao and L. Mai, Intricate Hollow Structures: Controlled Synthesis and Applications in Energy Storage and Conversion, *Adv. Mater.*, 2017, **29**, 1602914.
84 B. Peng, Z. Zhou, J. Shi, X. Huang, Y. Li and L. Ma, Earth-Abundant Fe-Mn-Based Compound Cathodes for Sodium-Ion Batteries: Challenges and Progress, *Adv. Funct. Mater.*, 2024, **34**, 2311816.
85 W. Shu, J. Li, G. Zhang, J. Meng, X. Wang and L. Mai, Progress on Transition Metal Ions Dissolution Suppression Strategies in Prussian Blue Analogs for Aqueous Sodium-/Potassium-Ion Batteries, *Nano-Micro Lett.*, 2024, **16**, 128.
86 J. Sun, H. Ye, J. A. S. Oh, A. Plewa, Y. Sun, T. Wu, Q. Sun, K. Zeng and L. Lu, Elevating the discharge plateau of Prussian blue analogs through low-spin Fe redox induced intercalation pseudocapacitance, *Energy Storage Mater.*, 2021, **43**, 182–189.
87 Z. Wang, W. Zhuo, J. Li, L. Ma, S. Tan, G. Zhang, H. Yin, W. Qin, H. Wang, L. Pan, A. Qin and W. Mai, Regulation of ferric iron vacancy for Prussian blue analogue cathode to realize high-performance potassium ion storage, *Nano Energy*, 2022, **98**, 107243.
88 J. Song, L. Wang, Y. Lu, J. Liu, B. Guo, P. Xiao, J.-J. Lee, X.-Q. Yang, G. Henkelman and J. B. Goodenough, Removal of Interstitial H_2O in Hexacyanometallates for a Superior Cathode of a Sodium-Ion Battery, *J. Am. Chem. Soc.*, 2015, **137**, 2658–2664.
89 J. Wu, J. Song, K. Dai, Z. Zhuo, L. A. Wray, G. Liu, Z.-x. Shen, R. Zeng, Y. Lu and W. Yang, Modification of Transition-Metal Redox by Interstitial Water in Hexacyanometalate Electrodes for Sodium-Ion Batteries, *J. Am. Chem. Soc.*, 2017, **139**, 18358–18364.
90 Y. Huang, M. Xie, J. Zhang, Z. Wang, Y. Jiang, G. Xiao, S. Li, L. Li, F. Wu and R. Chen, A novel border-rich Prussian blue synthetized by inhibitor control as cathode for sodium ion batteries, *Nano Energy*, 2017, **39**, 273–283.
91 J. Peng, W. Zhang, Q. Liu, J. Wang, S. Chou, H. Liu and S. Dou, Prussian Blue Analogues for Sodium-Ion Batteries: Past, Present, and Future, *Adv. Mater.*, 2022, **34**, 2108384.
92 W. J. Li, C. Han, G. Cheng, S. L. Chou, H. K. Liu and S. X. Dou, Chemical Properties, Structural Properties, and Energy Storage Applications of Prussian Blue Analogues, *Small*, 2019, **15**, 1900470.
93 Y. Ma, Y. Ma, S. L. Dreyer, Q. Wang, K. Wang, D. Goonetilleke, A. Omar, D. Mikhailova, H. Hahn, B. Breitung and T. Brezesinski, High-Entropy Metal–Organic Frameworks for Highly Reversible Sodium Storage, *Adv. Mater.*, 2021, **33**, 2101342.
94 L. Zhang, C. Tsolakidou, S. Mariyappan, J.-M. Tarascon and S. Trabesinger, Unraveling gas evolution in sodium batteries by online electrochemical mass spectrometry, *Energy Storage Mater.*, 2021, **42**, 12–21.
95 M. He, R. Davis, D. Chartouni, M. Johnson, M. Abplanalp, P. Troendle and R. P. Suetterlin, Assessment of the first commercial Prussian blue based sodium-ion battery, *J. Power Sources*, 2022, **548**, 232036.
96 Z. Li, M. Dadsetan, J. Gao, S. Zhang, L. Cai, A. Naseri, M. E. Jimenez-Castaneda, T. Filley, J. T. Miller, M. J. Thomson and V. G. Pol, Revealing the Thermal Safety of Prussian Blue Cathode for Safer Nonaqueous Batteries, *Adv. Energy Mater.*, 2021, **11**, 2101764.
97 H. Gao, I. D. Seymour, S. Xin, L. Xue, G. Henkelman and J. B. Goodenough, $Na_3MnZr(PO_4)_3$: A High-Voltage Cathode for Sodium Batteries, *J. Am. Chem. Soc.*, 2018, **140**, 18192–18199.
98 K. Hurlbutt, S. Wheeler, I. Capone and M. Pasta, Prussian Blue Analogs as Battery Materials, *Joule*, 2018, **2**, 1950–1960.

99 H. Zhang, J. Li, J. Liu, Y. Gao, Y. Fan, X. Liu, C. Guo, H. Liu, X. Chen, X. Wu, Y. Liu, Q. Gu, L. Li, J. Wang and S.-L. Chou, Understanding capacity fading from structural degradation in Prussian blue analogues for wide-temperature sodium-ion cylindrical battery, *Nat. Commun.*, 2025, **16**, 2520.

100 X. Rong, D. Xiao, Q. Li, Y. Niu, F. Ding, X. Hou, Q. Wang, J. Xu, C. Zhao, D. Zhou, R. Xiao, X. Yu, W. Yin, L. Gu, H. Li, X. Huang, L. Chen and Y.-S. Hu, Boosting reversible anionic redox reaction with Li/Cu dual honeycomb centers, *eScience*, 2023, **3**, 100159.

101 C. Wang, J. T. Kim, C. Wang and X. Sun, Progress and Prospects of Inorganic Solid-State Electrolyte-Based All-Solid-State Pouch Cells, *Adv. Mater.*, 2023, **35**, 2209074.

102 B. Jia, B. Zhang, Z. Cai, X. Yang, L. Li and L. Guo, Construction of amorphous/crystalline heterointerfaces for enhanced electrochemical processes, *eScience*, 2023, **3**, 100112.

103 M. Cui, Y. Zhu, H. Lei, A. Liu, F. Mo, K. Ouyang, S. Chen, X. Lin, Z. Chen, K. Li, Y. Jiao, C. Zhi and Y. Huang, Anion–Cation Competition Chemistry for Comprehensive High-Performance Prussian Blue Analogs Cathodes, *Angew. Chem., Int. Ed.*, 2024, **63**, e202405428.

104 Y.-B. Niu, Y.-J. Guo, Y.-X. Yin, S.-Y. Zhang, T. Wang, P. Wang, S. Xin and Y.-G. Guo, High-Efficiency Cathode Sodium Compensation for Sodium-Ion Batteries, *Adv. Mater.*, 2020, **32**, 2001419.

105 X. Zhao, N. Liu, M. Zheng, X. Wang, Y. Xu, J. Liu, F. Li and L. Wang, Four-Electron Redox Reaction in Prussian Blue Analogue Cathode Material for High-Performance Sodium-Ion Batteries, *ACS Energy Lett.*, 2024, **9**, 2748–2757.

106 J. Zhang, J. Zhang, H. Wang, V. W.-h. Lau, G.-H. Lee, K. Zhang, M. Park and Y.-M. Kang, Solid–Solid Interfacial Charge Storage of Prussian Blue/rGO Mixed-Conductor Cathode for High-Power Na Ion Batteries, *ACS Energy Lett.*, 2022, **7**, 4472–4482.

107 S. Fan, Y. Gao, Y. Liu, L. Li, L. Zhang, Z. Zhou, S.-L. Chou, X. Liu, Y. Shen, Y. Huang and Y. Qiao, Recrystallization-Driven Quasi-Spherical Prussian Blue Analogs with High Tap Density and Crystallinity for Sodium-Ion Batteries, *ACS Energy Lett.*, 2025, **10**, 1751–1761.

108 N. Liu, Z. Lu, J. Zhao, M. T. McDowell, H.-W. Lee, W. Zhao and Y. Cui, A pomegranate-inspired nanoscale design for large-volume-change lithium battery anodes, *Nat. Nanotechnol.*, 2014, **9**, 187–192.

109 D. O. Ojwang, M. Svensson, C. Njel, R. Mogensen, A. S. Menon, T. Ericsson, L. Häggström, J. Maibach and W. R. Brant, Moisture-Driven Degradation Pathways in Prussian White Cathode Material for Sodium-Ion Batteries, *ACS Appl. Mater. Interfaces*, 2021, **13**, 10054–10063.

110 Z.-Y. Chen, X.-Y. Fu, L.-L. Zhang, B. Yan and X.-L. Yang, High-Performance Fe-Based Prussian Blue Cathode Material for Enhancing the Activity of Low-Spin Fe by Cu Doping, *ACS Appl. Mater. Interfaces*, 2022, **14**, 5506–5513.

111 Z. Xu, F. Chen, Y. Li, Y. Lu, A. Zhou, J. Jiang, X. Xu, J. Tu, B. Pan, F. Chen, Y. Huang, X. Zhao and J. Xie, A Self-Constructed Mg^{2+}/K^{+} Co-Doped Prussian Blue with Superior Cycling Stability Enabled by Enhanced Coulombic Attraction, *Adv. Sci.*, 2024, **11**, 2406842.

112 C.-C. Wang, L.-L. Zhang, X.-Y. Fu, H.-B. Sun and X.-L. Yang, Hollow Layered Iron-Based Prussian Blue Cathode with Reduced Defects for High-Performance Sodium-Ion Batteries, *ACS Appl. Mater. Interfaces*, 2024, **16**, 18959–18970.

113 W. Ren, M. Qin, Z. Zhu, M. Yan, Q. Li, L. Zhang, D. Liu and L. Mai, Activation of Sodium Storage Sites in Prussian Blue Analogues *via* Surface Etching, *Nano Lett.*, 2017, **17**, 4713–4718.

114 C. Xu, Y. Ma, J. Zhao, P. Zhang, Z. Chen, C. Yang, H. Liu and Y.-S. Hu, Surface Engineering Stabilizes Rhombohedral Sodium Manganese Hexacyanoferrates for High-Energy Na-Ion Batteries, *Angew. Chem., Int. Ed.*, 2023, **62**, e202217761.

115 Y. Zhang, X. Zhou, C. Yang, X. Liu, M. Wang, J. Han, H. Yan and Y. You, Air-Stable Prussian White Cathode Materials for Sodium-Ion Batteries Enabled by ZnO Surface Modification, *ACS Appl. Mater. Interfaces*, 2024, **16**, 15649–15656.

116 J. Sun, H. Ye, J. A. S. Oh, Y. Sun, A. Plewa, Y. Wang, T. Wu, K. Zeng and L. Lu, Alleviating mechanical degradation of hexacyanoferrate *via* strain locking during Na^{+} insertion/extraction for full sodium ion battery, *Nano Res.*, 2022, **15**, 2123–2129.

117 F. Feng, S. Chen, S. Zhao, W. Zhang, Y. Miao, H. Che, X.-Z. Liao and Z.-F. Ma, Enhanced electrochemical performance of MnFe@NiFe Prussian blue analogue benefited from the inhibition of Mn ions dissolution for sodium-ion batteries, *Chem. Eng. J.*, 2021, **411**, 128518.

118 X. Liu, J. Zhao, H. Dong, L. Zhang, H. Zhang, Y. Gao, X. Zhou, L. Zhang, L. Li, Y. Liu, S. Chou, W. Lai, C. Zhang and S. Chou, Sodium Difluoro(oxalato)borate Additive-Induced Robust SEI and CEI Layers Enable Dendrite-Free and Long-Cycling Sodium-Ion Batteries, *Adv. Funct. Mater.*, 2024, **34**, 2402310.

119 W. Kuang, X. Zhou, Z. Fan, X. Chen, Z. Yang, J. Chen, X. Shi, L. Li, R. Zeng, J.-Z. Wang and S. Chou, Sulfur-Containing Inorganic-Rich Interfacial Chemistry Empowers Advanced Sodium-Ion Full Batteries, *ACS Energy Lett.*, 2024, **9**, 4111–4118.

120 L. Ge, Y. Song, P. Niu, B. Li, L. Zhou, W. Feng, C. Ma, X. Li, D. Kong, Z. Yan, Q. Xue, Y. Cui and W. Xing, Elaborating the Crystal Water of Prussian Blue for Outstanding Performance of Sodium Ion Batteries, *ACS Nano*, 2024, **18**, 3542–3552.

121 M. Jiang, Z. Hou, J. Wang, L. Ren, Y. Zhang and J.-G. Wang, Balanced coordination enables low-defect Prussian blue for superfast and ultrastable sodium energy storage, *Nano Energy*, 2022, **102**, 107708.

122 Y. Wang, J. Liu, N. Jiang, J. Yang, C. Yang and Y. Liu, Highly Crystalline Multivariate Prussian Blue Analogs *via* Equilibrium Chelation Strategy for Stable and Fast Charging Sodium-Ion Batteries, *Small*, 2024, **20**, 2403211.

123 Y. Shang, X. Li, J. Song, S. Huang, Z. Yang, Z. J. Xu and H. Y. Yang, Unconventional Mn Vacancies in Mn-Fe

Prussian Blue Analogs: Suppressing Jahn-Teller Distortion for Ultrastable Sodium Storage, *Chem*, 2020, **6**, 1804–1818.

124 M. Wan, R. Zeng, J. Meng, Z. Cheng, W. Chen, J. Peng, W. Zhang and Y. Huang, Post-Synthetic and *In Situ* Vacancy Repairing of Iron Hexacyanoferrate Toward Highly Stable Cathodes for Sodium-Ion Batteries, *Nano-Micro Lett.*, 2021, **14**, 9.

125 Y. Zhu, Z. Zhang, J. Bao, S. Zeng, W. Nie, P. Chen, Y. Zhou and Y. Xu, Multi-metal doped high capacity and stable Prussian blue analogue for sodium ion batteries, *Int. J. Energy Res.*, 2020, **44**, 9205–9212.

126 T. Matsuda, J. E. Kim, K. Ohoyama and Y. Moritomo, Universal thermal response of the Prussian blue lattice, *Phys. Rev. B: Condens. Matter Mater. Phys.*, 2009, **79**, 172302.

127 F. Scholz and D. C. A. Dostal, The Formal Potentials of Solid Metal Hexacyanometalates, *Angew. Chem., Int. Ed. Engl.*, 1996, **34**, 2685–2687.

128 J. Zhang, J. Wan, M. Ou, S. Liu, B. Huang, J. Xu, S. Sun, Y. Xu, Y. Lin, C. Fang and J. Han, Enhanced all-climate sodium-ion batteries performance in a low-defect and Na-enriched Prussian blue analogue cathode by nickel substitution, *Energy Mater.*, 2023, **3**, 300008.

129 L.-L. Zhang, Z.-Y. Chen, X.-Y. Fu, B. Yan, H.-C. Tao and X.-L. Yang, Effect of Zn-substitution induced structural regulation on sodium storage performance of Fe-based Prussian blue, *Chem. Eng. J.*, 2022, **433**, 133739.

130 H. Zhang, J. Peng, L. Li, Y. Zhao, Y. Gao, J. Wang, Y. Cao, S. Dou and S. Chou, Low-Cost Zinc Substitution of Iron-Based Prussian Blue Analogs as Long Lifespan Cathode Materials for Fast Charging Sodium-Ion Batteries, *Adv. Funct. Mater.*, 2023, **33**, 2210725.

131 J. Peng, W. Hua, Z. Yang, J.-Y. Li, J. Wang, Y. Liang, L. Zhao, W. Lai, X. Wu, Z. Cheng, G. Peleckis, S. Indris, J.-Z. Wang, H. K. Liu, S. X. Dou and S. Chou, Structural Engineering of Prussian Blue Analogues Enabling All-Climate and Ultralong Cycling Sodium-Ion Batteries, *ACS Nano*, 2024, **18**, 19854–19864.

132 H. Fu, C. Liu, C. Zhang, W. Ma, K. Wang, Z. Li, X. Lu and G. Cao, Enhanced storage of sodium ions in Prussian blue cathode material through nickel doping, *J. Mater. Chem. A*, 2017, **5**, 9604–9610.

133 P. Jiang, H. Shao, L. Chen, J. Feng and Z. Liu, Ion-selective copper hexacyanoferrate with an open-framework structure enables high-voltage aqueous mixed-ion batteries, *J. Mater. Chem. A*, 2017, **5**, 16740–16747.

134 X. Liu, Y. Cao and J. Sun, Defect Engineering in Prussian Blue Analogs for High-Performance Sodium-Ion Batteries, *Adv. Energy Mater.*, 2022, **12**, 2202532.

135 C. Ling, J. Chen and F. Mizuno, First-Principles Study of Alkali and Alkaline Earth Ion Intercalation in Iron Hexacyanoferrate: The Important Role of Ionic Radius, *J. Phys. Chem. C*, 2013, **117**, 21158–21165.

136 C. D. Wessells, M. T. McDowell, S. V. Peddada, M. Pasta, R. A. Huggins and Y. Cui, Tunable reaction potentials in open framework nanoparticle battery electrodes for grid-scale energy storage, *ACS Nano*, 2012, **6**, 1688–1694.

137 S. Phadke, R. Mysyk and M. Anouti, Effect of cation (Li^+, Na^+, K^+, Rb^+, Cs^+) in aqueous electrolyte on the electrochemical redox of Prussian blue analogue (PBA) cathodes, *J. Energy Chem.*, 2020, **40**, 31–38.

138 J. Wang, Z. Yuan, J. Liao, A. Li, Y. Xu, H. Qi, Y. Man, Y. Lv and X. Zhou, Cesium-doped manganese-based Prussian blue analogue as a high-efficiency cathode material for potassium-ion batteries, *J. Energy Chem.*, 2024, **99**, 120–127.

139 X. Liu, H. Gong, C. Han, Y. Cao, Y. Li and J. Sun, Barium ions act as defenders to prevent water from entering Prussian blue lattice for sodium-ion battery, *Energy Storage Mater.*, 2023, **57**, 118–124.

140 A. Zhou, C. Guo, J. Jiang, D. Wang, X. Wang, S. Ali, J. Li, W. Xia, M. Fu and W. Sun, The Pillar Effect of Large-Size Alkaline Ions on the Electrochemical Stability of Sodium Manganese Hexacyanoferrate for Sodium-Ion Batteries, *Small*, 2023, **19**, 2304887.

141 Y. Gao, X. Wu, L. Wang, Y. Zhu, G. Sun, Y. Tang, M. Yan and Y. Jiang, Structurally Stable, Low H_2O Prussian Blue Analogs toward High Performance Sodium Storage, *Adv. Funct. Mater.*, 2024, **34**, 2314860.

142 H. Zhang, Y. Gao, J. Peng, Y. Fan, L. Zhao, L. Li, Y. Xiao, W. K. Pang, J. Wang and S. L. Chou, Prussian Blue Analogues with Optimized Crystal Plane Orientation and Low Crystal Defects toward 450 W h kg^{-1} Alkali-Ion Batteries, *Angew. Chem., Int. Ed.*, 2023, **62**, e202303953.

143 Q. Han, Y. Hu, S. Gao, Z. Yang, X. Liu, C. Wang and J. Han, Improved Reversible Capacity and Cycling Stability by Linear (N=O) Anions in $Fe[Fe(CN)_5NO]$ as Sodium-Ion Battery Cathode, *ChemSusChem*, 2023, **16**, e202300823.

144 H.-W. Lee, R. Y. Wang, M. Pasta, S. Woo Lee, N. Liu and Y. Cui, Manganese hexacyanomanganate open framework as a high-capacity positive electrode material for sodium-ion batteries, *Nat. Commun.*, 2014, **5**, 5280.

145 Q. Han, Z. Yang, Y. n. Hu, S. Gao, X. Liu, C. Wang and J. Han, Suppressing the Jahn–Teller effect in Mn-based Prussian blue analogues by linear (NO) anions, *Chem. Eng. J.*, 2024, **493**, 152575.

146 H. Furukawa, U. Müller and O. M. Yaghi, "Heterogeneity within Order" in Metal-Organic Frameworks, *Angew. Chem., Int. Ed.*, 2015, **54**, 3417–3430.

147 B. Xie, L. Wang, H. Li, H. Huo, C. Cui, B. Sun, Y. Ma, J. Wang, G. Yin and P. Zuo, An interface-reinforced rhombohedral Prussian blue analogue in semi-solid state electrolyte for sodium-ion battery, *Energy Storage Mater.*, 2021, **36**, 99–107.

148 Z. Wang, K. Luo, Y. Mo, J. Ke, W. Zhou, S. Chen, P. Gao and J. Liu, Synergistic Dual-Additive Tailored Robust Interphase toward Enhanced Cyclability of Prussian Blue Cathode for K^+ Storage, *Adv. Funct. Mater.*, 2025, **35**, 2417243.

149 Q. Liu, D. Zhang, Y. Yang, Y. Gu, Z. Liang, W. Chen, Y. Wu and L. Hu, Encapsulation of Prussian Blue Analogues with Conductive Polymers for High-Performance Ammonium-Ion Storage, *Adv. Energy Mater.*, 2025, **15**, 2402863.

150 X.-Y. Fu, L.-L. Zhang, Z.-Y. Chen, Y. Xu, J. Wu, C.-C. Wang, X.-K. Ding, X.-L. Yang and J. Lu, Achieving a superior Na storage performance of Fe-based Prussian blue cathode

by coating perylene tetracarboxylic dianhydride amine, *Carbon Energy*, 2024, **6**, e446.

151 Z.-X. Cai, Z.-L. Wang, J. Kim and Y. Yamauchi, Hollow Functional Materials Derived from Metal–Organic Frameworks: Synthetic Strategies, Conversion Mechanisms, and Electrochemical Applications, *Adv. Mater.*, 2019, **31**, 1804903.

152 H. Cheng, Y.-N. Liu, Z.-E. Yu, Y. Song, Y. Qin, M. Zhang, R. Chen, J. Zhou, Y. Liu and B. Guo, Ion exchange to construct a high-performance core–shell MnFe-PB@CuFe-PB cathode material for sodium ion batteries, *J. Mater. Chem. C*, 2023, **11**, 9787–9793.

153 X. Liu, X. Zheng, Y. Dai, B. Li, J. Wen, T. Zhao and W. Luo, Suppression of Interphase Dissolution *Via* Solvent Molecule Tuning for Sodium Metal Batteries, *Adv. Mater.*, 2023, **35**, 2304256.

154 Y. Gao, H. Zhang, J. Peng, L. Li, Y. Xiao, L. Li, Y. Liu, Y. Qiao and S.-L. Chou, A 30-year overview of sodium-ion batteries, *Carbon Energy*, 2024, **6**, e464.

155 J. Ge, L. Fan, A. M. Rao, J. Zhou and B. Lu, Surface-substituted Prussian blue analogue cathode for sustainable potassium-ion batteries, *Nat. Sustain.*, 2022, **5**, 225–234.

156 H. Zhang, H. Wang, W. Li, Y. Wei, B. Wen, D. Zhai and F. Kang, Enabling High-Performance Potassium-Ion Batteries by Manipulating Interfacial Chemistry, *Adv. Funct. Mater.*, 2024, **34**, 2312368.

157 H. Sun, G. Zhu, X. Xu, M. Liao, Y.-Y. Li, M. Angell, M. Gu, Y. Zhu, W. H. Hung, J. Li, Y. Kuang, Y. Meng, M.-C. Lin, H. Peng and H. Dai, A safe and non-flammable sodium metal battery based on an ionic liquid electrolyte, *Nat. Commun.*, 2019, **10**, 3302.

158 D. Zhang, J. Ma, C. Zhang, M. Liu, K. Yang, Y. Li, X. Cheng, Z. Wang, H. Wang, W. Lv, Y.-B. He and F. Kang, A novel cathode interphase formation methodology by preferential adsorption of a borate-based electrolyte additive, *Nat. Sci. Rev.*, 2024, **11**, 2095–5138.

159 J.-H. Kim, J.-H. Hyun, S. Kim, W. H. Park and S.-H. Yu, Phosphorus-Based Flame-Retardant Electrolytes for Lithium Batteries, *Adv. Energy Mater.*, 2025, 2500587.

160 Z. Yang, Y. Dai, Z.-K. Xie, S.-B. Li, Y.-J. Lei, J. Chen, X. Zhou, Z.-Q. Hao, X. Tan, L. Li, W.-H. Lai, L. Li, W.-H. Chen and S.-L. Chou, Modulating ion–dipole interactions in nonflammable phosphonate-based electrolyte for safe and stable sodium-ion pouch cells, *Nat. Sci. Rev.*, 2024, **12**, 2095–5138.

161 B. Xie, P. Zuo, L. Wang, J. Wang, H. Huo, M. He, J. Shu, H. Li, S. Lou and G. Yin, Achieving long-life Prussian blue analogue cathode for Na-ion batteries *via* triple-cation lattice substitution and coordinated water capture, *Nano Energy*, 2019, **61**, 201–210.

162 Z.-Y. Chen, L.-L. Zhang, X.-Y. Fu, B. Yan and X.-L. Yang, Synergistic Modification of Fe-Based Prussian Blue Cathode Material Based on Structural Regulation and Surface Engineering, *ACS Appl. Mater. Interfaces*, 2022, **14**, 43308–43318.

163 X. Xu, Y. Lan, B. Zhang, S. Zhu, Y. Yang and Y. Gao, Construction of polyaniline coated FeMnCu co-doped Prussian blue analogue as cathode for sodium ion battery, *Electrochim. Acta*, 2023, **471**, 143375.